Publ. Astron. Soc. Japan (2022) 74 (5), 1234–1262
https://doi.org/10.1093/pasj/psac067
Advance Access Publication Date: 2022 September 5

Millimeter methanol emission in the high-mass young stellar object G24.33+0.14

Tomoya Hirota [1,2,*] Pawel Wolak [3] Todd R. Hunter [4,5] Crystal L. Brogan [4] Anna Bartkiewicz [3] Michal Durjasz [3] Agnieszka Kobak [3] Mateusz Olech [6] Marian Szymczak [3] Ross A. Burns [1,7] Artis Aberfelds [8] Giseon Baek [9] Jan Brand [10] Shari Breen [11] Do-Young Byun [7] Alessio Caratti o Garatti [12] Xi Chen [13] James O. Chibueze [14,15] Claudia Cyganowski [16] Jochen Eislöffel [17] Simon Ellingsen [18] Naomi Hirano [19] Bo Hu [20,21] Ji-hyun Kang [7] Jeong-Sook Kim [22] Jungha Kim [7] Kee-Tae Kim [7] Mi Kyoung Kim [23] Busaba Kramer [24,25] Jeong-Eun Lee [9] Hendrik Linz [26] Tie Liu [27] Gordon MacLeod [28,29] Tiege P. McCarthy [18] Karl Menten [24] Kazuhito Motogi [30] Chung-Sik Oh [7] Gabor Orosz [18,31] Andrey M. Sobolev [32] Bringfried Stecklum [17] Koichiro Sugiyama [1,25] Kazuyoshi Sunada [33,34] Lucero Uscanga [35] Fanie van den Heever [29] Alexandr E. Volvach [36] Larisa N. Volvach [36] Yuan Wei Wu [37] and Yoshinori Yonekura [38]

[1]National Astronomical Observatory of Japan, 2-21-1 Osawa, Mitaka-shi, Tokyo 181-8588, Japan
[2]Department of Astronomical Sciences, SOKENDAI (The Graduate University for Advanced Studies), 2-21-1 Osawa, Mitaka-shi, Tokyo 181-8588, Japan
[3]Institute of Astronomy, Faculty of Physics, Astronomy and Informatics, Nicolaus Copernicus University, Grudziadzka 5, PL-87-100 Torun, Poland
[4]NRAO, 520 Edgemont Road, Charlottesville, VA 22903, USA
[5]Center for Astrophysics | Harvard-Smithsonian, 60 Garden Street, Cambridge, MA 02138, USA
[6]Space Radio-Diagnostic Research Center, Faculty of Geoengineering, University of Warmia and Mazury, Olsztyn 10-710, Poland
[7]Korea Astronomy and Space Science Institute, 776 Daedeokdaero, Yuseong, Daejeon 34055, Republic of Korea
[8]Engineering Research Institute, Ventspils International Radio Astronomy Center, Ventspils University of Applied Sciences, Inzenieru Str. 101, Ventspils, LV-3601, Latvia
[9]School of Space Research, Kyung Hee University, 1732, Deogyeong-daero, Giheung-gu, Yongin-si, Gyeonggi-do 17104, Republic of Korea
[10]INAF-Istituto di Radioastronomia and Italian ALMA Regional Centre, via P. Gobetti 101, 40129 Bologna, Italy
[11]SKAO, Jodrell Bank, Lower Withington, Macclesfield, Cheshire SK11 9FT, UK
[12]INAF-Osservatorio Astronomico di Capodimonte, Salita Moiariello, 16, 80131, Napoli, Italy
[13]Center for Astrophysics, Guangzhou University, Guangzhou 510006, China
[14]Centre for Space Research, Physics Department, North-West University, Potchefstroom 2520, South Africa

[15]Department of Physics and Astronomy, Faculty of Physical Sciences, University of Nigeria, Carver Building, 1 University Road, Nsukka, Nigeria
[16]SUPA, School of Physics and Astronomy, University of St. Andrews, North Haugh, St. Andrews KY16 9SS, UK
[17]Thüringer Landessternwarte, Sternwarte 5, 07778 Tautenburg, Germany
[18]School of Natural Sciences, University of Tasmania, Private Bag 37, Hobart, Tasmania 7001, Australia
[19]Institute of Astronomy and Astrophysics, Academia Sinica, 11F of Astronomy-Mathematics Building, AS/NTU, No.1, Sec. 4, Roosevelt Rd, Taipei 10617, Taiwan
[20]School of Astronomy and Space Science, Nanjing University, 163 Xianlin Avenue, Nanjing 210023, China
[21]Key Laboratory of Modern Astronomy and Astrophysics (Nanjing University), Ministry of Education, Nanjing 210023, China
[22]Ulsan National Institute of Science and Technology UNIST-gil 50, Eonyang-eup, Ulju-gun, Ulsan 44919, Republic of Korea
[23]Department of Child Studies, Faculty of Home Economics, Otsuma Women's University, 12 Sanban-cho, Chiyoda-ku, Tokyo 102-8357, Japan
[24]Max-Planck-Institut für Radioastronomie, Auf dem Hügel 69, 53121 Bonn, Germany
[25]National Astronomical Research Institute of Thailand (Public Organization), 260 Moo 4, T. Donkaew, Amphur Maerim, Chiang Mai, 50180, Thailand
[26]Max-Planck-Institut für Astronomie, Königstuhl 17, D-69117 Heidelberg, Germany
[27]Key Laboratory for Research in Galaxies and Cosmology, Shanghai Astronomical Observatory, Chinese Academy of Sciences, 80 Nandan Road, Shanghai 200030, China
[28]The University of Western Ontario, 1151 Richmond Street, London, ON N6A 3K7, Canada
[29]South African Radio Astronomy Observatory, Hartebeesthoek site, PO Box 443, Krugersdorp 1740, South Africa
[30]Graduate School of Sciences and Technology for Innovation, Yamaguchi University, 1677-1 Yoshida, Yamaguchi, Yamaguchi 753-8512, Japan
[31]Joint Institute for VLBI ERIC, Oude Hoogeveensedijk 4, 7991 PD Dwingeloo, Netherlands
[32]Astronomical Observatory, Institute for Natural Sciences and Mathematics, Ural Federal University, 19 Mira street, Ekaterinburg, 620002, Russia
[33]National Astronomical Observatory of Japan, Hoshigaoka 2-12, Mizusawa, Oshu-shi, Iwate 023-0861, Japan
[34]Department of Astronomical Sciences, SOKENDAI (The Graduate University for Advanced Studies), 2-12 Hoshigaoka, Mizusawa, Oshu-shi, Iwate 023-0861, Japan
[35]Department of Astronomy, University of Guanajuato, Apartado Postal 144, 36000 Guanajuato, Gto, Mexico
[36]Radio Astronomy and Geodynamics Department of Crimean Astrophysical Observatory, Katsively, RT-22 Crimea
[37]National Time Service Center, Key Laboratory of Precise Positioning and Timing Technology, Chinese Academy of Sciences, Xi'an 710600, China
[38]Center for Astronomy, Ibaraki University, 2-1-1 Bunkyo, Mito, Ibaraki 310-8512, Japan

*E-mail: tomoya.hirota@nao.ac.jp

Received 2022 February 21; Accepted 2022 July 28

Abstract

In 2019 September, a sudden flare of the 6.7 GHz methanol maser was observed toward the high-mass young stellar object (HMYSO) G24.33+0.14. This may represent the fourth detection of a transient mass accretion event in an HMYSO after S255IR NIRS3, NGC 6334I-MM1, and G358.93−0.03-MM1. G24.33+0.14 is unique among these sources as it clearly shows a repeating flare with an 8 yr interval. Using the Atacama Large Millimeter/submillimeter Array (ALMA), we observed the millimeter continuum and molecular lines toward G24.33+0.14 in the pre-flare phase in 2016 August (ALMA Cycle 3) and the mid-flare phase in 2019 September (ALMA Cycle 6). We identified three continuum sources in G24.33+0.14, and the brightest source, C1, which is closely associated with

the 6.7 GHz maser emission, shows only a marginal increase in flux density with a flux ratio (Cycle 6/Cycle 3) of 1.16 ± 0.01, considering an additional absolute flux calibration uncertainty of 10%. We identified 26 transitions from 13 molecular species other than methanol, and they exhibit similar levels of flux differences with an average flux ratio of 1.12 ± 0.15. In contrast, eight methanol lines observed in Cycle 6 are brighter than those in Cycle 3 with an average flux ratio of 1.23 ± 0.13, and the higher excitation lines tend to show a larger flux increase. If this systematic increasing trend is real, it would suggest radiative heating close to the central HMYSO due to an accretion event which could expand the size of the emission region and/or change the excitation conditions. Given the low brightness temperatures and small flux changes, most of the methanol emission is likely to be predominantly thermal, except for the 229.759 GHz (8_{-1}–7_0 E) line known as a class I methanol maser. The flux change in the millimeter continuum of G24.33+0.14 is smaller than in S255IR NIRS3 and NGC 6334I-MM1 but is comparable with that in G358.93−0.03-MM1, suggesting different amounts of accreted mass in these events.

Key words: masers — radio lines:ISM — stars: formation — stars: individual (G24.33+0.14) — stars: protostars

1 Introduction

Recent high angular resolution observations have made significant contributions to the understanding of the high-mass star-formation process. Remarkable recent observational results are the discovery of accretion burst events in two high-mass young stellar objects (HMYSOs), S255IR NIRS 3 (Caratti o Garatti et al. 2017; Cesaroni et al. 2018; Liu et al. 2018, 2020; Szymczak et al. 2018b; Uchiyama et al. 2020; Hirota et al. 2021) and NGC 6334I-MM1 (Hunter et al. 2017, 2018, 2021; Brogan et al. 2018; MacLeod et al. 2018; Chibueze et al. 2021). Multi-wavelength observations in these two sources showed that the continuum emission from millimeter to infrared wavelengths increased due to the change in accretion luminosity of HMYSOs by a factor of 5.5 (S255IR NIRS3) and 16.3 (NGC 6334I-MM1). The estimated mass accretion rate is as high as $>10^{-3}\,M_{\odot}\,\mathrm{yr}^{-1}$ over a much shorter timescale (i.e., of the order of months or years) than the entire lifetime of HMYSOs ($\sim 10^4$ yr). This can be interpreted as episodic mass accretion caused by disk fragmentation. Theoretical models suggest that HMYSOs undergo a number of such episodic mass accretion bursts during their formation (Meyer et al. 2017, 2019, 2021; Elbakyan et al. 2021). Despite their importance for the understanding of the high-mass star-formation process, observed examples of accretion bursts are still rare.

The accretion events in S255IR NIRS3 and NGC 6334I-MM1 were both accompanied by sudden flaring of the methanol (CH_3OH) maser line of the 5_1–6_0 A^+ transition at 6.7 GHz (hereafter referred to as the 6.7 GHz methanol masers) as reported by many monitoring and mapping observations (Fujisawa et al. 2015; Moscadelli et al. 2017; Hunter et al. 2018; MacLeod et al. 2018; Szymczak et al. 2018b). Methanol masers are divided into two classes. Class I masers are collisionally pumped within the shocked gas by the interaction of the molecular outflows with the ambient gas at a variety of distances from protostars, while class II masers are radiatively excited by the strong infrared radiation field (Cragg et al. 2005) located only in close proximity of HMYSOs (Breen et al. 2013) tracing circumstellar gas of disks or outflow cavities (Menten 1991). The 6.7 GHz methanol emission is the representative transition of the class II methanol maser line. Thus, the above results suggest that the 6.7 GHz methanol maser flare is caused by a luminosity change due to an accretion burst; the increased accretion luminosity heats the surrounding dust which leads to increased emission of infrared photons, and hence increased 6.7 GHz methanol maser emission via the radiative pumping mechanism. In addition, it has also been reported that some pre-existing maser features disappear during the accretion bursts, due to the introduction of unfavorable conditions of maser pumping (Moscadelli et al. 2017; Hunter et al. 2018). Since maser emission is a non-linear phenomenon and is very sensitive to the physical environment, it can be used as a probe to detect the onset of accretion burst events.

With this in mind, a collaboration team "Maser Monitoring Organization (M2O)"[1] was organized in 2017 September during the International Astronomical Union (IAU) Symposium 336 "Astrophysical Masers" in Cagliari, Italy. One of the purposes of the M2O is to detect maser

[1] ⟨https://www.masermonitoring.org⟩.

flares using a global collaborative network of radio telescopes. Indeed, the M2O activity succeeded in identifying the third candidate of a possible mass accretion event in an HMYSO, G358.93−0.03-MM1, in 2019 January based on the 6.7 GHz methanol maser flare (Sugiyama et al. 2019), followed by monitoring observations to obtain detailed maser light curves (MacLeod et al. 2019; Volvach et al. 2020).

Follow-up target-of-opportunity (ToO) observations of G358.93−0.03-MM1 have identified the possible candidate HMYSO undergoing the accretion burst from the Atacama Large Millimeter/submillimeter Array (ALMA) observation in Director's Discretionary Time (DDT) (Brogan et al. 2019). Very-long-baseline interferometry (VLBI) imaging reveals a change in the radius of the shell-like maser distribution from 260 to 520 au within one month (Burns et al. 2020), implying that the location of the maser emitting region changes due to the heating from the central protostar. This finding, as well as the detection of a far-infrared luminosity increase (Stecklum et al. 2021), confirmed the presence of an accretion burst. In addition, a number of methanol maser lines were detected toward G358.93−0.03-MM1 including very rare and first-time detected transitions (Breen et al. 2019; Brogan et al. 2019; Chen et al. 2020), suggesting changes in the physical properties of the surrounding media as reported for the 6.7 GHz methanol masers in S255IR NIRS3 and NGC 6334I-MM1 (Moscadelli et al. 2017; Hunter et al. 2018). Another 6.7 GHz methanol maser flare which is proposed to have been caused by an accretion event has been reported in the HMYSO G323.459−0.079 (Proven-Adzri et al. 2019; MacLeod et al. 2021), as verified by the 2.2 μm near-infrared light curve (V. Wolf in preparation).

In addition, the 22.2 GHz water (H_2O) maser line of the $6_{1,6}$–$5_{2,3}$ transition (hereafter the 22.2 GHz water maser) is known to be highly variable, and sometimes to show strong flares associated with shocks induced by outflows in accretion burst sources (e.g., NGC 6334I-MM1; Brogan et al. 2018; MacLeod et al. 2018; Chibueze et al. 2021). According to variabilities in the 22.2 GHz water maser and mid-infrared continuum emission, an HMYSO M 17 MIR is also suggested to have experienced multiple accretion burst events (Chen et al. 2021). Thus, the number of possible candidates for accretion bursts in HMYSOs is increasing. Remarkably, the intermediate-mass YSO G107.298+5.639 shows joint periodic infrared and methanol maser flares (Stecklum et al. 2018), possibly due to binary-induced modulation of the accretion rate.

On 2019 September 5, the M2O reported a new 6.7 GHz methanol maser flare in the star-forming region G24.33+0.14 using the Torun 32 m radio telescope as

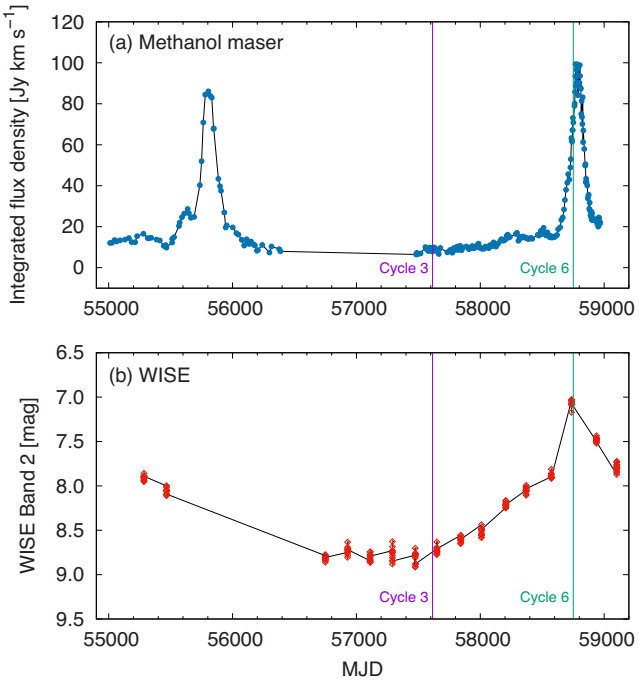

Fig. 1. Light curves of G24.33+0.14. (a) Flux density of the 6.7 GHz methanol maser line integrated over the whole velocity range (Wolak et al. 2019, A. Kobak, in preparation). Observations were conducted with the Torun 32 m radio telescope. (b) Multi-epoch photometry data of WISE/NEOWISE Band 2 at the wavelength of 4.6 μm (Wright et al. 2010; Mainzer et al. 2011). Vertical lines indicate the dates of our ALMA observations in ALMA Cycle 3 and Cycle 6.

shown in figure 1 (Wolak et al. 2019). The multi-frequency studies characterized the spatial structure and evolution of the methanol and water masers during this flare (A. Kobak, in preparation) . The integrated flux density increased from 20 to 100 Jy between ∼2019 June and October (between ∼58600 and 58800 in MJD), and the main contribution to the velocity-integrated flux density comes from two features near 113.5 km s^{-1} and 115.4 km s^{-1} (Wolak et al. 2019). This maser has previously been observed to show flaring activity between 2010 and 2012 (between ∼55500 and 56000 in MJD), in which almost all spectral features had shown similar flare profiles but with significant time delays between features/velocities (Wolak et al. 2018).

Long-term monitoring observations toward G24.33+0.14 revealed that the 6.7 GHz methanol maser shows variability with a strong flare lasting 200–400 d (Szymczak et al. 2018a). Since the WISE/NEOWISE infrared fluxes rose along with the onset of the recent maser flare (figure 1), an accretion burst origin seems likely. It is worth mentioning that G24.33+0.14 clearly shows a repeating nature of the 6.7 GHz methanol maser flare (figure 1). Monitoring observations of maser flares can provide insight into the physical mechanisms of the 6.7 GHz methanol maser flares and their periodicity.

Fortunately, G24.33+0.14 was observed in the pre-flare phase in ALMA Cycle 3 at ∼0.″3 resolution in 2016 August, which corresponds to a linear scale of 2200 au at the estimated distance of 7.2 kpc (see subsection 1.1). Thus, this is an ideal target to compare the millimeter continuum emission and molecular lines both before and during the flare phases. In this paper, we report observational studies of G24.33+0.14 using ALMA Cycle 3 and newly obtained ALMA Cycle 6 DDT observations at Band 6 (230 GHz or $\lambda = 1.4$ mm).

1.1 Target source

G24.33+0.14 is an HMYSO located at an estimated distance of $D = 7.20 \pm 0.76$ kpc (Reid et al. 2016) according to their Bayesian distance estimator.[2] It has been identified as a hot molecular core in an infrared dark cloud (IRDC) associated with a compact millimeter core MM1 observed with the Plateau de Bure Interferometer (PdBI) of Institut de Radioastronomie Millimétrique (IRAM) and the Submillimeter Array (SMA) at resolutions of 1″–2″ and 0.″6, respectively (Rathborne et al. 2007, 2011). The estimated luminosity, diameter, and mass of the core are $10^{4.8}\,L_\odot$, 0.0128 pc, and 34 $M_\odot$ (Rathborne et al. 2011).[3] The spectral energy distribution (SED) from millimeter to mid-infrared wavelengths at lower resolution gives a similar luminosity of $10^{4.7}\,L_\odot$ and a larger clump mass of 3088 $M_\odot$ (Sánchez-Monge et al. 2013),[4] which is also consistent with the presence of (a) HMYSO(s). Single-dish mapping observations of the SiO and HCO^+ lines with the IRAM 30 m telescope with resolutions of 28″ at 90 GHz and 10″ at 230 GHz revealed a molecular outflow along the north–south or north-west–south-east direction in which the northern lobe shows a redshifted component (Sánchez-Monge et al. 2013). G24.33+0.14 is associated with an EGO (extended green object) detected by SPITZER with emission at 4.5μm of shocked H_2 molecules (Cyganowski et al. 2008; Chambers et al. 2009).

The 6.7 GHz methanol masers were observed using the Australia Telescope Compact Array (ATCA) to measure their accurate positions (Caswell 2009; Xu et al. 2009; Breen et al. 2015) at absolute positional accuracy of ∼0.″4. The 6.7 GHz methanol masers were also imaged by the European VLBI Network (EVN; Bartkiewicz et al. 2016), and the Jansky Very Large Array (JVLA; Hu et al. 2016) in the pre-flare phase. There are three spatial groups of maser features where the size of the distributions is ∼0.″5 or 3600 au at a distance of 7.2 kpc. Another class I methanol maser emission at 95.2 GHz (8_0–7_1 A^+ transition) was detected, but the spatial distribution has not yet been determined (Chen et al. 2011).

The 22.2 GHz water masers were detected in the pre-flare phase (Caswell & Green 2011; Cyganowski et al. 2013). After the onset of the 6.7 GHz methanol maser flare, this source was observed with ATCA, and the 22.2 GHz water, the 23.4 GHz methanol maser (10_1–9_2 A^-) and the 4.8 GHz H_2CO maser ($1_{1,0}$–$1_{1,1}$) were also detected in 2019 November (McCarthy et al. 2022). The 23.4 GHz methanol maser and the 4.8 GHz H_2CO maser are the fourth and 11th example of these rare maser transitions, respectively, and hence they could suggest maser pumping during the accretion event similar to G358.93−0.03-MM1 (Breen et al. 2019; Brogan et al. 2019; Chen et al. 2020). The positions of the H_2O and H_2CO masers are coincident with those of the 6.7 GHz methanol maser within their astrometric accuracy (0.″5 and 3″ in right ascension and declination, respectively), while the 23.4 GHz methanol masers are shifted to 7″ north and 2″ west (McCarthy et al. 2022).

2 Observations and data analysis

2.1 ALMA observations in Cycle 3 and Cycle 6

The observations in the pre-flare phase were conducted with ALMA in Cycle 3 (2015.1.01571.S), as a part of a survey of millimeter methanol maser lines in high-mass star-forming regions. Key parameters in the observations are listed in table 1. There were three individual observing sessions on 2016 August 15, 19, and 22 using 38, 39, and 40 12 m antennas, respectively. The baseline length ranged from 15.1 m to 1.5 km in each of the three sessions and the corresponding uv coverage is shown in figure 2. The tracking center position of G24.33+0.14 was taken to be RA = $18^h35^m07^s.800$ and Dec = −07°35′06.″00 (J2000.0). The net on-source time on G24.33+0.14 was 18 min, comprising 18 1 min scans (six scans in each session). Amplitude calibration was obtained by observing J1733−1304 or J1924−2914. As discussed in the Appendix, the absolute flux calibration accuracy is estimated to be 10%. Bandpass and phase calibrators were J1751+0939 and J1851+0035, respectively. The ALMA Band 6 receiver was used to cover portions of the frequency range from 213 GHz to 231 GHz (see table 1 for details). The primary beam size of the 12 m antenna is 25″–27″ at the observing frequency.

Just 20 days after the onset of the maser flare, additional data was obtained in Cycle 6 (2018.A.00068.T) as

[2] We employ a systemic velocity of 113.5 ± 0.6 km s^{-1} determined from the average velocity of the detected methanol lines. See ⟨http://bessel.vlbi-astrometry.org⟩ for more detailed information.

[3] Rathborne et al. (2011) estimated the luminosity, diameter, and mass assuming a distance of 6.3 kpc. We corrected these values by multiplying by a factor of 1.1 for the diameter and 1.3 for the mass and luminosity using the distance of 7.2 kpc.

[4] Similarly, we corrected the luminosity and mass by multiplying by a factor of 1.2 as Sánchez-Monge et al. (2013) used the distance of 6.7 kpc.

Table 1. Observational parameters.

	ALMA Cycle 3	ALMA Cycle 6
Project code	2015.1.01571.S	2018.A.00068.T
Date	2016 August 15, 19, and 22	2019 September 25 and 26
Number of antennas	38, 39, 40	45
Baseline length	15.1 m–1.5 km	15.1 m–2.5 km
Amplitude calibrator	J1733−1304 or J1924−2914	J1924−2914
Bandpass calibrator	J1751+0939	J1924−2914
Phase calibrator	J1851+0035	J1832−1035
SPW 0*	213.343 GHz, 937.50 MHz, 976.562 kHz	213.337 GHz, 468.75 MHz, 244.141 kHz
SPW 1*	217.020 GHz, 937.50 MHz, 976.562 kHz	217.013 GHz, 468.75 MHz, 244.141 kHz
SPW 2*	229.668 GHz, 468.75 MHz, 976.562 kHz	229.662 GHz, 468.75 MHz, 244.141 kHz
Velocity resolution	1.27–1.38 km s^{-1}	0.32–0.34 km s^{-1}

*Center frequency, bandwidth, and spectral resolution of each spectral window (spw).

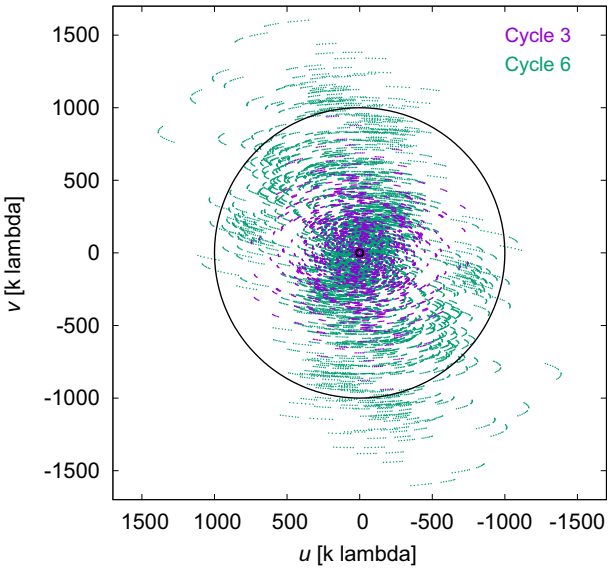

Fig. 2. *uv* coverage of the ALMA observations carried out in Cycle 3 (purple) and Cycle 6 (green). Small and large black circles indicate the *uv* range used in the imaging between 25 kλ and 1000 kλ, respectively.

an ALMA DDT project. Details of observations are also summarized in table 1. Observations were conducted from 2019 September 25 to 26 consisting of two sessions. The number of 12 m antennas was 45, with baseline lengths from 15.1 m to 2.5 km. The *uv* coverage in the observation, along with that in Cycle 3, is plotted in figure 2. Based on the previous observations in Cycle 3, the tracking center position of G24.33+0.14 was shifted to the continuum peak of RA = $18^{h}35^{m}08^{s}.140$ and Dec = $-07^{\circ}35'04''.15$ (J2000.0) by (+5″.06, +1″.85) with respect to that in the Cycle 3 observations. The net on-source time was 96 min, consisting of 12 8 min scans (six scans in each session). Amplitude and bandpass calibration were performed by observing J1924−2914 and phase calibration was performed using J1832−1035. The ALMA Band 6 receiver was used to cover frequency ranges similar to those employed in the Cycle 3 observations but at higher spectral resolution, and hence narrower bandwidths (for details see table 1).

2.2 Data analysis

For both the Cycle 3 and Cycle 6 projects, the pipeline script provided by the EA-ARC (East-Asian ALMA Regional Center) was used to calibrate the visibility data. Synthesis imaging and self-calibration were done using the CASA (Common Astronomy Software Applications) software package (McMullin et al. 2007) versions 4.7.0 and 5.6.1 for Cycle 3 and Cycle 6 data, respectively. The pipeline versions employed in the data analysis were r38377 and r42866, respectively. Continuum images were produced using line-free channels in all spectral windows (spws) and were used in self-calibration. Both phase and amplitude solutions were determined in self-calibration, and these solutions were applied to both the continuum and continuum-subtracted spectral line data. The spectral line images were made by smoothing the velocity resolution to 1.5 km s^{-1} and 0.5 km s^{-1} for Cycle 3 and Cycle 6 data, respectively, to investigate velocity structures of detected methanol transitions. However, image cubes were made using the same velocity resolution of 1.5 km s^{-1} to compare the Cycle 3 and Cycle 6 results. In order to compare the flux densities and peak intensities between Cycle 3 and Cycle 6 as accurately as possible, a common *uv* range of (25–1000) kλ was employed (figure 2), for both the Cycle 3 and Cycle 6 data in the synthesis imaging. The shortest *uv* distance on 25 kλ corresponds to the spatial scale of 8″. Using a Briggs robust weighting parameter of 0.5, the resultant beam sizes of the continuum images were 0″.26 × 0″.24 with a position angle of −87° and 0″.22 × 0″.17 with a position angle of −74° for Cycle 3 and Cycle 6 data, respectively. These were convolved to the same beam size of 0″.3

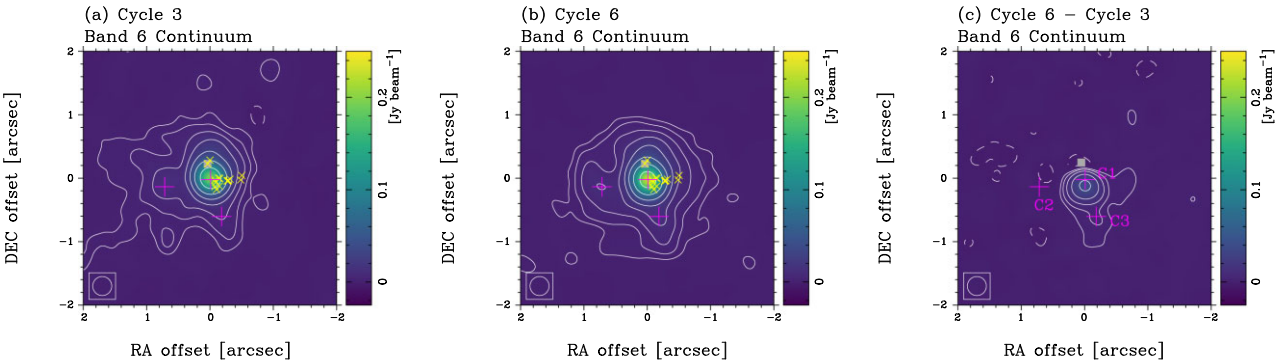

Fig. 3. ALMA Band 6 continuum ($\lambda = 1.4$ mm) images for (a) Cycle 3, (b) Cycle 6, and (c) their differential image. Contour levels are $-4, 4, 8, 16, \ldots$, 512 times the rms noise level of 0.45 mJy beam^{-1} and 0.32 mJy beam^{-1} for the Cycle 3 and Cycle 6 data, respectively. Dashed contours indicate negative levels. The rms noise level of the differential image is 0.55 mJy beam^{-1}. All panels employ the same color scale. Magenta crosses indicate the positions of the continuum peaks, C1, C2, and C3. Yellow X symbols represent the positions of the 6.7 GHz methanol maser cloudlets observed with the VLBA and a gray square indicates the position of the flaring maser feature (A. Kobak in preparation). The (0, 0) position corresponds to RA = $18^{h}35^{m}08^{s}.140$ and Dec = $-07^{\circ}35'04''.15$ (J2000.0) .

using the same velocity resolution of 1.5 km s^{-1} in the following discussion. Part of the image analysis and plotting was done using the National Radio Astronomy Observatory (NRAO) Astronomical Image Processing System (AIPS) software package (Greisen 2003).

For the ALMA Cycle 3 and Cycle 6 data, a visibility amplitude calibration error is known to impact some observations.[5] This was caused by the combined effect of correlator spectral normalization and Tsys (system noise temperature) calibration. We checked the possible effect of this amplitude calibration error and found that the differences are less than 1% (typically 0.1%–0.5%) for both continuum and target spectral lines in both Cycle 3 and Cycle 6 observations. Thus, the effect on our analysis is negligible and we have utilized the originally delivered data before correction of this amplitude calibration error.

3 Results

3.1 Continuum emission

Figure 3 depicts the continuum emission measured in ALMA Band 6 in both Cycle 3 and Cycle 6 using the same *uv* ranges and convolved beam size of 0.″3. The continuum emission shows almost the same spatial structure with marginally resolved peak emission and a diffuse component extending toward the eastern side of the core. The maps reveal multiple continuum components. We conducted multiple 2D Gaussian fitting to the images of both Cycle 3 and Cycle 6 data. As a result, we identify three continuum peaks, C1, C2, and C3. Their properties are summarized in table 2.

All the components including the marginal structure of C3 can be fitted consistently in both Cycle 3 and Cycle 6 data. The separations of C2 and C3 with respect to C1 are 5000 au (0.″7) and 4000 au (0.″6), respectively. The continuum positions measured in Cycle 6 are offset to the south by 0.″02–0.″04 compared with those in Cycle 3. These differences can be regarded as uncertainty in the astrometry of the ALMA data. The brightest peak, C1, carries 80% of the total continuum flux density, while the two weaker peaks, C2 and C3, are identified to the east and south of C1, respectively, with signal-to-noise ratios greater than 50. The position of C1 is coincident with the 6.7 GHz methanol maser feature at (0.″0361, 0.″2258) or the absolute coordinate of (RA = $18^{h}35^{m}08^{s}.14243$, Dec = $-07^{\circ}35'03''.9242$) measured through phase-referencing VLBI astrometry with the Very Long Baseline Array (VLBA) (A. Kobak in preparation). C2 is well resolved from C1, while C3 is seen as a spur extending from the southern part of C1. The nature of C3 is unclear because of the limited spatial resolution. After subtracting three Gaussian components corresponding to C1, C2, and C3 from the images, there still remain two residual components both in the Cycle 3 and Cycle 6 data, located at 0.″5 north and 0.″5 west of C1 with the maximum intensities of 19 mJy beam^{-1} and 8 mJy beam^{-1}, respectively.

A previous interferometer observation at 1.3 mm with PdBI in 2005 reported a flux density of 284.0 mJy with an uncertainty of 10% (Rathborne et al. 2007). While the spatial resolution with the PdBI (1.″5 × 0.″8) was much lower than that of the ALMA observations (0.″3), and hence only a single component was identified, the flux density measured with the PdBI is 78% of the ALMA result of the brightest component C1 in the pre-flare phase in 2013. The difference could be attributed to the larger missing flux in the PdBI data because its shortest baseline length of 48 m,

[5] ⟨https://almascience.nao.ac.jp/news/amplitude-calibration-issue-affecting-some-alma-data⟩.

Table 2. Properties of the continuum emission.

Source ID	Cycle	ΔRA, ΔDec (″, ″)*	F (mJy)	$F_{\rm Cycle\,6}/F_{\rm Cycle\,3}$ ratio	I (mJy beam^{-1})	T_B (K)†	$I_{\rm Cycle\,6}/I_{\rm Cycle\,3}$ ratio	M ($M_\odot$)‡	Size, PA (″ × ″, °)	Deconvolved size, PA (″ × ″, °)
G24.33+0.14 C1	3	−0.0106(3), 0.0051(3)	336(1)	—	187.6(4)	52.6(1)	—	54.4(2)	0.413(1) × 0.390(1), 27(1)	0.284(2) × 0.250(2), 27(2)
	6	−0.0108(3), −0.0221(3)	390(1)	1.16(1)	218.3(3)	61.2(1)	1.16(1)	63.1(2)	0.413(1) × 0.389(1), 19(1)	0.284(1) × 0.248(1), 19(1)
G24.33+0.14 C2	3	0.677(9), −0.093(10)	54(2)	—	10.9(4)	3.0(1)	—	8.7(3)	0.742(24) × 0.599(20), 21(6)	0.680(34) × 0.519(30), 21(8)
	6	0.714(11), −0.136(10)	54(2)	1.01(5)	9.9(3)	2.8(1)	0.91(4)	8.8(3)	0.859(28) × 0.573(19), 53(3)	0.805(39) × 0.488(29), 53(4)
G24.33+0.14 C3	3	−0.195(12), −0.583(10)	25(2)	—	7.6(4)	2.1(1)	—	4.0(2)	0.600(28) × 0.494(23), 82(10)	0.519(43) × 0.392(39), 82(13)
	6	−0.185(7), −0.603(7)	43(2)	1.71(9)	11.7(3)	3.3(1)	1.55(9)	6.8(2)	0.583(16) × 0.559(16), 13(27)	0.500(25) × 0.472(24), 13(35)

*Position offset with respect to the phase center of RA = $18^{\rm h}35^{\rm m}08\overset{\rm s}{.}140$ and Dec = −07°35′04″.15. The numbers in parentheses represent the fitting errors (1σ) in units of the last significant digits.
†The brightness temperature is converted from the peak intensity value.
‡The dust temperature is fixed to 100 K.

which corresponds to the angular scale of 6″ (Rathborne et al. 2007), is slightly longer than that employed in our ALMA imaging of 35 m (25 kλ). Since the upper-side-band frequency of the PdBI of 219.560 GHz was only lower by 0.2% than our average frequency of 220.010 GHz for the three spws, the frequency difference will not significantly affect the flux mismatch.

The difference in the continuum emission between Cycle 3 and Cycle 6 is shown in panel (c) of figure 3. The difference map shows a peak at 0.″1 south of the brightest component, C1. Between the 2016 August and 2019 September ALMA observations, both the flux density and peak intensity of C1 appear to increase by a factor of 1.16 ± 0.01 (Cycle 6/Cycle 3). C3 also shows a flux difference between Cycle 3 and Cycle 6, although the measured flux densities could not be fully distinguished from those of C1. If we consider C3 as a part of a single source, the flux ratio for C1 + C3 between Cycle 3 and Cycle 6 is calculated at 1.20 ± 0.01, which is slightly higher than that for only C1 (1.16 ± 0.01). On the other hand, the flux density of the more isolated component C2 appears to be unchanged. As noted above, the residual components at the north and east of C1 are unchanged in intensities between Cycle 3 and Cycle 6, and hence there is no corresponding component in the differential image (figure 3c). We have checked for possible contamination or residual from line emission by constructing synthesized images of the continuum-subtracted visibility using only line-free channels and find that it is less than 0.015 mJy beam^{-1} or 0.2%. Considering additional contributions of absolute flux calibration uncertainties of 10% and a slight difference in the *uv* coverage between Cycle 3 and Cycle 6 data, the flux increase in C1 from Cycle 3 to Cycle 6 is marginal.[6]

While it is difficult to measure continuum opacity only from our ALMA Band 6 data, the beam-averaged brightness temperature of ∼50–60 K would suggest a moderate or low opacity given the gas temperature of >100 K inferred from the methanol line brightness temperatures (table 3). If the dust continuum emission is optically thin, the mass of each continuum source can be estimated using $M = FD^2/[\kappa_\nu B_\nu(T_{\rm dust})]$, where F is the integrated flux density listed in table 2, D is the distance of 7.2 kpc, and $B_\nu(T_{\rm dust})$ is the Planck function at the dust temperature of $T_{\rm dust}$. For consistency, we assumed a dust opacity of $\kappa_\nu = 1.0\,{\rm cm^2\,g^{-1}}$ at 230 GHz (Ossenkopf & Henning 1994), a gas-to-dust ratio of 100, and $T_{\rm dust}$ of 100 K, as employed in Rathborne, Simon, and Jackson (2007) and Rathborne et al. (2011). If we assumed a higher dust temperature of 150–300 K, then the estimated masses would be reduced by a factor of 1.5–3. On the other hand,

[6] ⟨https://almascience.eso.org/documents-and-tools/cycle6/alma-proposers-guide⟩.

Table 3. Line parameters of the methanol transitions.*

Transition	$\nu^{\dagger}$ (GHz)	$E_u{}^{\ddagger}$ (K)	$S\mu^{2\S}$ (D^2)	Cycle	$F_{peak}{}^{\|}$ (Jy)	$F_{Cycle\,6}/F_{Cycle\,3}$ ratio	$I_{peak}{}^{\sharp}$ (Jy beam^{-1})	$T_B{}^{**}$ (K)	$I_{Cycle\,6}/I_{Cycle\,3}$ ratio	$v_{peak}{}^{\dagger\dagger}$ (km s^{-1})	$\Delta v_{peak}{}^{\dagger\dagger}$ (km s^{-1})	Distribution,‡‡ maser class§§
CH_3OH $v_t = 0$												
13_6–14_5 E	213.377528	389.92	10.18	3	1.72(8)	—	0.32(2)	95(5)	—	114.2(1)	4.1(2)	Compact
				6	2.15(7)	1.25(7)	0.41(1)	122(3)	1.29(9)	114.0(1)	4.4(2)	—
1_1–0_0 E	213.427061	23.37	3.57	3	2.96(13)	—	0.30(1)	88(3)	—	114.1(1)	5.0(3)	Extended
				6	3.47(17)	1.17(8)	0.37(2)	111(4)	1.26(7)	114.2(1)	5.0(3)	Class II [a]
5_1–4_2 E	216.945521	55.87	4.49	3	2.79(12)	—	0.37(1)	107(3)	—	113.8(1)	5.7(3)	Extended
				6	3.35(20)	1.20(9)	0.56(2)	162(5)	1.52(7)	113.8(2)	5.6(4)	Class II [a]
15_4–16_3 E	229.589056	374.44	18.34	3	2.19(15)	—	0.39(1)	100(3)	—	113.7(2)	5.2(4)	Compact
				6	2.91(18)	1.33(12)	0.56(1)	144(3)	1.43(6)	113.8(2)	5.5(4)	Class II [b]
8_{-1}–7_0 E	229.758756	89.10	20.19	3	2.92(15)	—	0.25(1)	64(2)	—	114.2(1)	5.5(3)	Extended
				6	2.84(12)	0.97(7)	0.26(1)	66(2)	1.04(6)	114.3(1)	5.6(3)	Class I [c]
19_5–20_4 A$^-$	229.939095	578.60	22.79	3	1.36(5)	—	0.31(1)	78(3)	—	113.9(1)	4.8(2)	Compact
				6	1.76(8)	1.29(8)	0.41(2)	104(4)	1.32(8)	113.9(1)	4.4(2)	—
CH_3OH $v_t = 1$												
6_1–7_2 A$^-$	217.299205	373.92	18.66	3	2.27(5)	—	0.41(1)	117(2)	—	113.7(1)	5.2(1)	Compact
				6	3.26(11)	1.44(6)	0.57(2)	163(4)	1.39(5)	114.0(1)	4.7(2)	Class II [b]
$^{13}CH_3OH$ $v_t = 0$												
14_1–13_2 A$^-$	217.044616	254.25	5.79	3	0.84(6)	—	0.18(1)	50(3)	—	114.0(1)	3.7(3)	Extended
				6	1.01(5)	1.20(10)	0.20(1)	57(3)	1.14(10)	114.0(1)	3.9(2)	Class I^{J} [d]

*The numbers in parenthesis represent the uncertainties in units of the last significant digits.

†The rest frequencies of methanol transitions taken from CDMS (Müller et al. 2001).

‡Upper state energy level taken from CDMS (Müller et al. 2001).

§Intrinsic line strength and magnetic dipole moment taken from CDMS (Müller et al. 2001).

$^{\|}$Integrated flux density at the peak channel over 2″ × 2″ region around the C1 peak.

$^{\sharp}$Peak intensity at the peak channel around the C1 peak.

**The brightness temperature converted from the peak intensity value.

††Peak velocities and velocity width (full-width at half-maximum) determined by the Gaussian fitting of the integrated flux spectrum (figure 5).

‡‡The lines with "compact" are detected only around the continuum peak (2″ × 2″) while transitions with "extended" are distributed outside the continuum source extending in the north-west–south-east outflow lobes. Lines identified candidate class I or class II masers based on previous observations or theoretical models are indicated.

§§References: [a] Cragg et al. (2005). [b] Brogan et al. (2019). [c] Slysh et al. (2002). [d] Voronkov et al. (2012) but for the same transition of $^{12}CH_3OH$ line at 236.9 GHz.

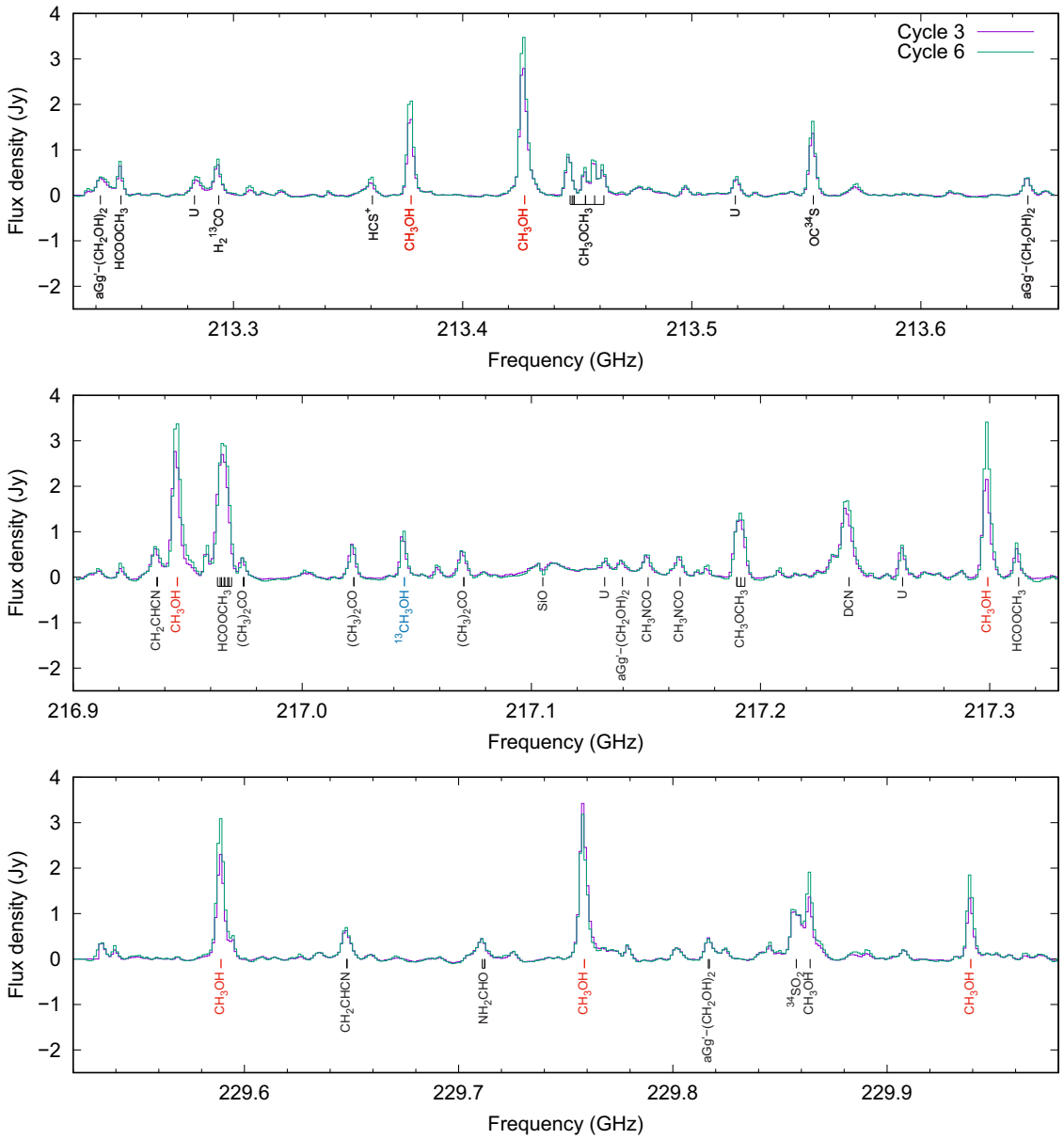

Fig. 4. All spectra observed within the common frequency range in both Cycle 3 (purple) and Cycle 6 (green). Flux densities are integrated over $2'' \times 2''$ around the brightest continuum source C1. Common *uv* range, convolved beam size, and spectral resolution are employed to produce image cubes for comparison (see subsection 2.2). "U" means an unidentified line (see table 4).

the core masses of C2 and C3 could be underestimated if they are colder prestellar cores, given the non-detection of the high excitation methanol line toward these positions (see subsection 3.3). Assuming the lower temperature of 20–50 K for these cores, the masses would become larger by a factor of 2–5. The estimated core masses are listed in table 2. Even considering the above uncertainties, these cores are potential sites of future and on-going high-mass star-formation with masses of about 10 $M_\odot$ or larger.

There is no other continuum emission source within the field of view, with the 3σ mass detection limit of 1 $M_\odot$ (assuming a dust temperature of 20 K).

3.2 Molecular line spectra

Observed spectra within the common frequency range in both Cycle 3 and Cycle 6 are shown in figure 4. The spectra were extracted by integrating the $2'' \times 2''$ region around the brightest continuum peak C1 of the channel maps. G24.33+0.14 is known as a hot molecular core, because higher-excitation lines of various complex organic molecules (COMs) consisting of more than six atoms (Herbst & van Dishoeck 2009) have been detected (Rathborne et al. 2011). Detected lines are identified based on the JPL Molecular Spectroscopy database (Pickett et al.

1998)[7] and the Cologne Database for Molecular Spectroscopy (CDMS; Müller et al. 2001),[8] as listed in table 3 for methanol and in table 4 for other molecules. Four lines, not identified with known molecular lines, are indicated as "unidentified" in table 4. We will not include these unidentified lines in the following statistical discussion. In the present paper, we focus on eight selected methanol lines including candidates of the class I and class II masers as summarized in table 3, including one torsionally excited line ($v_t = 1$) and one ^{13}C isotopologue. We note that there is one more identified CH_3OH line at 229.864121 GHz (19_5–20_4 A^+). However, this line is not included in the detailed analysis because it is partially blended with the nearby $^{34}SO_2$ line (see figure 4). Further detailed chemical properties of G24.33+0.14 along with other HMYSO samples (Baek et al. 2022) will be reported in forthcoming papers.

The strongest methanol emission in the current observations for both Cycle 3 and Cycle 6 is from the $v_t = 0$, 8_{-1}–7_0 E transition at 229.759 GHz, which has been identified as a class I methanol maser in other high-mass star-forming regions (Slysh et al. 2002; Cyganowski et al. 2011, 2012; Hunter et al. 2014; Kim et al. 2020). Two of the other lines, $v_t = 0$, 1_1–0_0 E at 213.427 GHz and $v_t = 0$, 5_1–4_2 E at 216.946 GHz, are predicted to be class II methanol masers (Cragg et al. 2005). Two other lines, $v_t = 1$, 6_1–7_2 A^- at 217.299 GHz and 15_4–16_3 E at 229.589 GHz, were detected in the 6.7 GHz methanol maser flare source, G358.93−0.03-MM1 (Brogan et al. 2019), and were assigned as class II methanol masers given their detection close to the continuum peak. It should be noted that the 217.299 GHz ($v_t = 1$, 6_1–7_2 A^-) line is the only transition associated with a torsionally excited state in our detected methanol lines. Regarding the $^{13}CH_3OH$ $v_t = 0$, 14_1–13_2 A^- line at 217.045 GHz, the corresponding transition of $^{12}CH_3OH$ at 236.9 GHz is listed as a class I methanol maser candidate (Voronkov et al. 2012). Thus, theoretical predictions, in which the counterpart $^{13}CH_3OH$ transitions tend to have similar propensity to the $^{12}CH_3OH$ masers (Johns et al. 1998), and observational confirmation (Chen et al. 2020) suggest that the 217.045 GHz (14_1–13_2 A^-) $^{13}CH_3OH$ transition is also a class I methanol maser candidate. On the other hand, we can find no publication which classifies the remaining two observed methanol transitions, CH_3OH $v_t = 0$, 13_6–14_5 E at 213.378 GHz and $v_t = 0$, 19_5–20_4 A^- at 229.939 GHz, as likely to be either class I or class II methanol maser transitions.

The flux densities are computed for all of the detected methanol lines integrated only around the continuum peak C1 ($2'' \times 2''$) and covering the whole emission region ($11'' \times 8''$) as plotted by solid and dashed lines, respectively, in figure 5. All the spectra are extracted from the channel maps presented in figures 6–8. The spectra have single Gaussian profiles with a weak blue wing suggesting a high-velocity component. The average peak LSR velocity is calculated to be 113.5 km s^{-1} with a standard deviation of 0.6 km s^{-1} at the continuum peak position, which is the same as the systemic velocity determined in previous observations (Rathborne et al. 2011).

Except for the 229.759 GHz (8_{-1}–7_0 E) line, the measured flux densities do not strongly depend on the size of the integrated regions. This means that most of the methanol lines except that of 229.759 GHz (8_{-1}–7_0 E) are emitted from the continuum peak position. In contrast, the 229.759 GHz (8_{-1}–7_0 E) line is much brighter when the emission is integrated over the larger region. Furthermore, the integrated flux density is 5–10 times larger than those of other lines as plotted in figure 5. As discussed later, the 229.759 GHz (8_{-1}–7_0 E) line shows a strong maser emission in the north-western lobe of the outflow in G24.33+0.14 (figure 8).

By comparing the methanol spectra between those in Cycle 3 and Cycle 6 in figure 5, a possible signature of a systematic increasing trend is seen in the flux densities. The ratios of the flux densities at the peak channel integrated over the $2'' \times 2''$ region of the eight methanol lines (Cycle 6/Cycle 3) range from 0.97 ± 0.07 to 1.44 ± 0.06 as listed in table 3, with a mean and standard deviation of 1.23 and 0.13, respectively. When we consider the flux density ratios integrated over the full linewidths, the average and standard deviation are in good agreement; 1.24 ± 0.12. The peak intensity ratios at the peak channel exhibit almost the same trend, with a mean and standard deviation of 1.30 and 0.15, respectively, and ranging from 1.04 ± 0.06 to 1.52 ± 0.07. It is noteworthy that the class I methanol maser transition at 229.759 GHz (8_{-1}–7_0 E) has the lowest flux ratio of 0.97 ± 0.07 (or the peak intensity ratio of 1.04 ± 0.06), and hence is an outlier on the low side. The difference between the methanol emission in the two epochs appears to be larger than that of the continuum emission of 1.16 ± 0.01 (Cycle 6/Cycle 3). We have determined that the uncertainty in the flux density due to continuum subtraction is less than 0.015 mJy beam^{-1}, and hence has negligible impact on the measurement of the line intensity.

Similar to the methanol lines, the integrated flux ratios between Cycle 3 and Cycle 6 data are measured for 26 identified transitions from 13 molecular species other than methanol, the integrated flux densities of which are higher than 0.3 Jy, to achieve higher signal-to-noise ratios than ∼10, as summarized in table 4. The average and standard

[7] ⟨https://spec.jpl.nasa.gov⟩.

[8] ⟨https://cdms.astro.uni-koeln.de⟩.

Table 4. Identified lines.

Molecule	ν^* (GHz)	Transition	$E_u{}^\dagger$ (K)	$F_{\mathrm{Cycle\,6}}{}^{\ddagger\S}$ (Jy)	$F_{\mathrm{Cycle\,6}}/F_{\mathrm{Cycle\,3}}{}^{\S}$ ratio	Reference$^\parallel$
aGg'-$(CH_2OH)_2$	213.2418954	$20_{6,15}(v=1)$–$19_{6,14}(v=0)$	121.61	0.38(3)	1.07(10)	CDMS
$HCOOCH_3$	213.2509190	$18_{3,16}$–$17_{3,15}$ A, $v_t=1$	292.89	0.68(10)	1.18(24)	JPL
Unidentified	213.283	—	—	0.36(2)	1.23(9)	—
$H_2{}^{13}CO$	213.2935650	$3_{3,1}$–$2_{2,0}$	67.77	0.72(6)	1.09(13)	CDMS
HCS^+	213.3606500	5–4	30.72	0.36(3)	1.67(24)	CDMS
CH_3OCH_3	213.4469319	$25_{4,22}$–$24_{5,19}$ AA	319.21	0.91(17)	1.14(31)	JPL
CH_3OCH_3	213.4477853	$25_{4,22}$–$24_{5,19}$ EE	319.21	—	—	JPL
CH_3OCH_3	213.4486380	$25_{4,22}$–$24_{5,19}$ EA	319.21	—	—	JPL
CH_3OCH_3	213.4486395	$25_{4,22}$–$24_{5,19}$ AE	319.21	—	—	JPL
CH_3OCH_3	213.4536380	$21_{1,20}$–$21_{0,21}$ AE	212.92	0.61(4)	1.17(13)	JPL
CH_3OCH_3	213.4536380	$21_{1,20}$–$21_{0,21}$ EA	212.92	—	—	JPL
CH_3OCH_3	213.4576210	$21_{1,20}$–$21_{0,21}$ EE	212.92	0.85(4)	1.21(11)	JPL
CH_3OCH_3	213.4616280	$21_{1,20}$–$21_{0,21}$ AA	212.92	0.69(4)	1.17(12)	JPL
Unidentified	213.519	—	—	0.36(2)	1.23(6)	—
$OC^{34}S$	213.5530610	18–17	97.37	1.60(5)	1.10(4)	JPL
aGg'-$(CH_2OH)_2$	213.6466934	$20_{6,14}(v=1)$–$19_{6,13}(v=0)$	121.65	0.38(2)	0.95(5)	CDMS
CH_2CHCN	216.9367119	$23_{2,22}$–$22_{2,21}$, $F=23$–22	133.93	0.57(6)	1.10(18)	JPL
CH_2CHCN	216.9367136	$23_{2,22}$–$22_{2,21}$, $F=22$–21	133.93	—	—	JPL
CH_2CHCN	216.9367182	$23_{2,22}$–$22_{2,21}$, $F=24$–23	133.93	—	—	JPL
$HCOOCH_3$	216.9629890	$20_{0,20}$–$19_{1,19}$ E	111.50	—	—	JPL
$HCOOCH_3$	216.9641571	$20_{0,20}$–$19_{1,19}$ A	111.48	—	—	JPL
$HCOOCH_3$	216.9647650	$20_{1,20}$–$19_{1,19}$ E	111.50	—	—	JPL
$HCOOCH_3$	216.9659004	$20_{1,20}$–$19_{1,19}$ A	111.48	3.05(12)	1.08(6)	JPL
$HCOOCH_3$	216.9662462	$20_{0,20}$–$19_{0,19}$ E	111.50	—	—	JPL
$HCOOCH_3$	216.9674200	$20_{0,20}$–$19_{0,19}$ A	111.48	—	—	JPL
$HCOOCH_3$	216.9679947	$20_{1,20}$–$19_{0,19}$ E	111.50	—	—	JPL
$HCOOCH_3$	216.9691890	$20_{1,20}$–$19_{0,19}$ A	111.48	—	—	JPL
$(CH_3)_2CO$	216.9744254	$19_{3,16}$–$18_{4,15}$ AE	115.56	0.39(7)	1.05(25)	JPL
$(CH_3)_2CO$	216.9744254	$19_{4,16}$–$18_{3,15}$ AE	115.56	—	—	JPL
$(CH_3)_2CO$	216.9744635	$19_{3,16}$–$18_{4,15}$ EA	115.56	—	—	JPL
$(CH_3)_2CO$	216.9744635	$19_{4,16}$–$18_{3,15}$ EA	115.56	—	—	JPL
$(CH_3)_2CO$	217.0225087	$19_{3,16}$–$18_{4,15}$ EE	115.50	0.71(3)	0.98(5)	JPL
$(CH_3)_2CO$	217.0225087	$19_{4,16}$–$18_{3,15}$ EE	115.50	—	—	JPL
$(CH_3)_2CO$	217.0705038	$19_{3,16}$–$18_{4,15}$ AA	115.43	0.59(2)	1.06(5)	JPL
$(CH_3)_2CO$	217.0705038	$19_{4,16}$–$18_{3,15}$ AA	115.43	—	—	JPL
SiO	217.1049800	5–4	31.26	0.26(2)	0.94(7)	JPL
Unidentified	217.132	—	—	0.45(1)	1.08(3)	—
aGg'-$(CH_2OH)_2$	217.1397235	$21_{4,17}(v=0)$–$20_{4,16}(v=1)$	123.93	0.32(3)	1.00(14)	CDMS
CH_3NCO	217.1509320	$25_{2,23}$–$24_{2,22}$, $m=0$	159.26	0.47(3)	1.13(13)	CDMS
CH_3NCO	217.1648810	$25_{-3,0}$–$24_{-3,0}$, $m=1$	200.96	0.42(4)	1.04(12)	CDMS
CH_3OCH_3	217.1896770	$22_{4,19}$–$22_{3,20}$ EA	253.41	—	—	JPL
CH_3OCH_3	217.1896770	$22_{4,19}$–$22_{3,20}$ AE	252.41	—	—	JPL
CH_3OCH_3	217.1914240	$22_{4,19}$–$22_{3,20}$ EE	252.41	1.47(6)	1.08(7)	JPL
CH_3OCH_3	217.1931700	$22_{4,19}$–$22_{3,20}$ AA	252.41	—	—	JPL
DCN	217.2384000	$J=3$–2, $F=2$–1	20.85	1.63(10)	1.12(9)	JPL
DCN	217.2386307	$J=3$–2, $F=2$–2	20.85	—	—	JPL
DCN	217.2386307	$J=3$–2, $F=3$–3	20.85	—	—	JPL
DCN	217.2386307	$J=3$–2, $F=3$–2	20.85	—	—	JPL
DCN	217.2386307	$J=3$–2, $F=4$–3	20.85	—	—	JPL

Table 4. (Continued)

Molecule	ν^* (GHz)	Transition	$E_u{}^\dagger$ (K)	$F_{\mathrm{Cycle\,6}}{}^{\ddagger\S}$ (Jy)	$F_{\mathrm{Cycle\,6}}/F_{\mathrm{Cycle\,3}}{}^{\S}$ ratio	Reference$^\parallel$
Unidentified	217.262	—	—	0.64(3)	1.13(8)	—
$HCOOCH_3$	217.3126260	$17_{4,13}$–$16_{4,12}$ A, $v_t = 1$	289.96	0.72(3)	1.17(8)	JPL
CH_2CHCN	229.6478347	$25_{1,25}$–$24_{1,24}$, $F = 24$–23	145.92	0.65(3)	1.06(7)	JPL
CH_2CHCN	229.6478354	$25_{1,25}$–$24_{1,24}$, $F = 25$–24	145.92	—	—	JPL
CH_2CHCN	229.6478396	$25_{1,25}$–$24_{1,24}$, $F = 26$–25	145.92	—	—	JPL
NH_2CHO	229.7109900	$10_{2,9}$–$10_{1,10}$, $F = 10$–10	67.80	—	—	JPL
NH_2CHO	229.7121192	$10_{2,9}$–$10_{1,10}$, $F = 11$–11	67.80	0.41(3)	1.08(11)	JPL
NH_2CHO	229.7122327	$10_{2,9}$–$10_{1,10}$, $F = 9$–9	67.80	—	—	JPL
aGg'-$(CH_2OH)_2$	229.8165729	$23_{9,15}(v=0)$–$22_{9,14}(v=1)$	175.60	0.44(3)	1.05(10)	CDMS
aGg'-$(CH_2OH)_2$	229.8171110	$23_{9,14}(v=0)$–$22_{9,13}(v=1)$	175.60	—	—	CDMS
$^{34}SO_2$	229.8576301	$4_{2,2}$–$3_{1,3}$	18.70	1.17(10)	1.06(12)	JPL
CH_3OH	229.8641210	19_5–20_4 A^+	578.60	1.71(11)	1.45(14)	JPL

*Transition rest frequency.
†Upper state energy level.
‡Flux density at the peak channel in Cycle 6 data with the resolution of 1.5 km s^{-1}. The numbers in parenthesis represent the formal uncertainties of the Gaussian fitting in units of the last significant digits.
§Lines blended with nearby other transition(s) are indicated as "—."
‖Pickett et al. (1998) and Müller et al. (2001) for JPL and CDMS, respectively.

deviation of the flux ratio (Cycle 6/Cycle 3) for a total of 26 lines other than methanol are 1.12 and 0.15, respectively. This ratio is comparable to the continuum flux ratio of 1.16 ± 0.01 but is smaller than that for the methanol lines of 1.23 ± 0.13. The average ratio for four unidentified lines, 1.17 ± 0.06, is almost the same as that for the 26 identified molecular lines.

Except for the eight analyzed methanol lines, the minimum and maximum ratios are 0.94 ± 0.07 (SiO) and 1.67 ± 0.24 (HCS^+), respectively. The next largest flux ratios after HCS^+ are 1.45 ± 0.14 for the methanol line at 229.864 GHz (19_5–20_4 A^+), which is not discussed above, and 1.21 ± 0.11 for the CH_3OCH_3 line at 213.458 GHz. We note that the HCS^+ line does not have a Gaussian line profile, and, moreover, a contribution from extended emission of HCS^+ is more significant than in the other spectral lines. The peak intensity ratio of the HCS^+ line, 0.85 ± 0.05, is half of the integrated flux density ratio. Although the same convolved beam size of 0.″3, *uv* range of (25–1000) kλ, and velocity resolution of 1.5 km s^{-1} are used to compare results between Cycle 3 and Cycle 6 as discussed in subsection 2.2, we cannot fully rule out possibilities of different effects of these observational settings on the flux increase in Cycle 6 with respect to those of Cycle 3, such as a difference in the maximum recoverable scale (MRS) relevant for extended emission. Except for HCS^+, the average flux ratio between Cycle 6 and Cycle 3 would be systematically larger for methanol lines than those of the other molecular lines and continuum emission.

3.3 Spatial structure of the methanol lines

In figures 6, 7, and 8, we present moment 0 and moment 1 maps for the Cycle 3 data to show spatial and velocity structures, a moment 0 map for the Cycle 6 data to show spatial structure more clearly, and the differential images of the moment 0 maps between Cycle 3 and Cycle 6 for two representative lines at 229.589 GHz (15_4–16_3 E) and 229.759 GHz (8_{-1}–7_0 E). For other lines, only moment 0 maps observed in Cycle 6, corresponding to panels (b) in figures 6–8, are presented in figure 9 for comparison. Because the velocity structures in Cycle 3 and Cycle 6 do not show significant differences, we only present the moment 1 maps for the Cycle 3 data. Channel maps from 106.5 to 123.0 km s^{-1} with A velocity resolution of 1.5 km s^{-1} are shown for Cycle 3, Cycle 6, and their differential images.

The spatial distribution of the methanol lines can be classified into two types, noted as "Compact" or "Extended" in table 3. "Compact" indicates a line showing an emission feature only around the continuum peak C1, such as the 213.378 GHz (13_6–14_5 E), 217.299 GHz ($v_t = 1$, 6_1–7_2 A^-), 229.589 GHz (15_4–16_3 E), and 229.939 GHz (19_5–20_4 A^-) lines. These lines are in a high rotational excitation state or torsionally excited state ($v_t = 1$). As a representative transition, moment maps of the $v_t = 0$, 15_4–16_3 E transition at 229.589 GHz are shown in figure 6, and the others are given in figures 9a–9c. Two of them, the 217.299 GHz ($v_t = 1$, 6_1–7_2 A^-) and 229.589 GHz (15_4–16_3 E) lines, are proposed to be class II methanol masers in G358.93−0.03-MM1 due to their very high observed brightness temperatures in this source (Brogan et al. 2019).

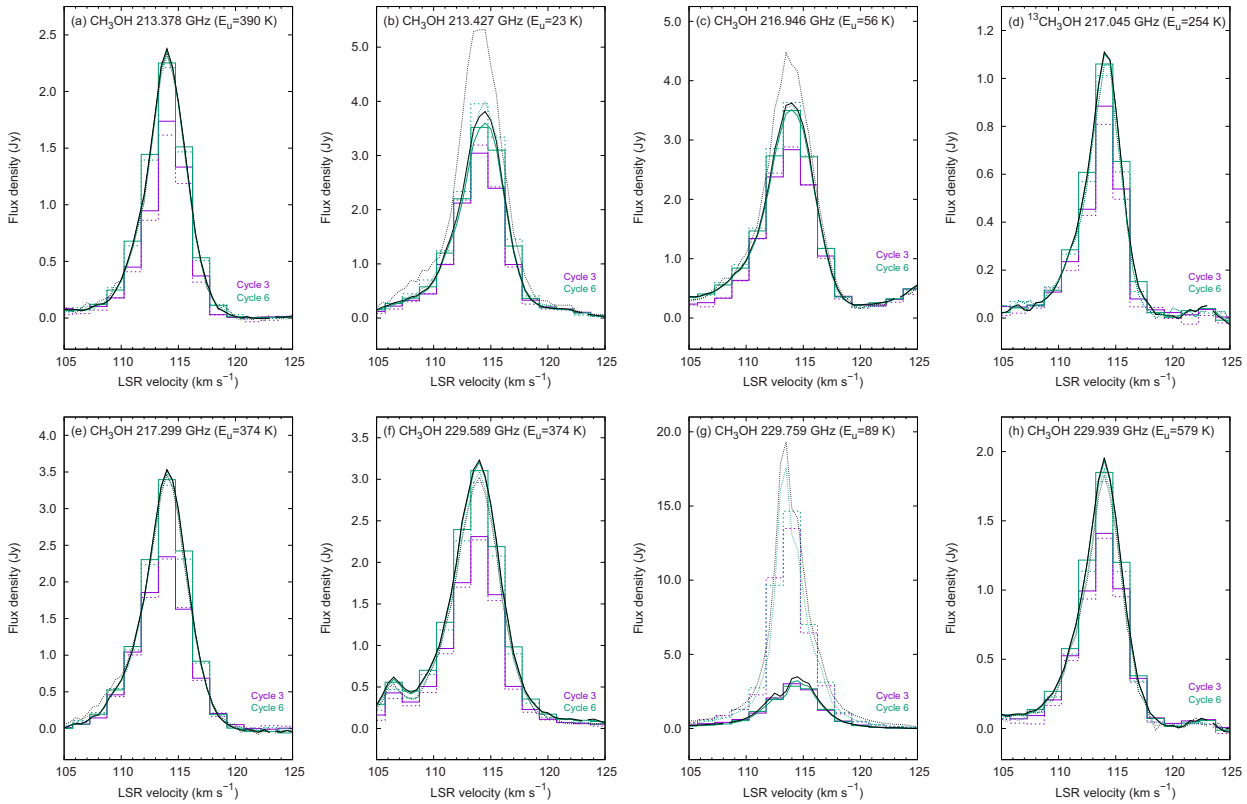

Fig. 5. Spectra of the observed methanol lines in both Cycle 3 (purple) and Cycle 6 (green). Solid lines show the spectra integrated over $2'' \times 2''$ around the brightest continuum emission peak C1 while dashed lines are extracted by integrating over $11'' \times 8''$ covering the whole emission region. Bold histograms are the spectra with the velocity resolution of 1.5 km s^{-1} while thin lines show the finer resolution Cycle 6 data with the resolution of 0.5 km s^{-1}. Images cubes used the common *uv* range and convolved beam size (see subsection 2.2).

The other methanol transitions, classified as "Extended", show elongated distributions along the north-west and south-east directions (e.g., along the outflow direction), as seen in the 213.427 GHz (1_1–0_0 E), 216.946 GHz (5_1–4_2 E), and 229.759 GHz (8_{-1}–7_0 E) lines. Examples of moment maps for the $v_t = 0$, 8_{-1}–7_0 E transition at 229.759 GHz are presented in figures 7 and 8. The rest of the two lines are mapped in figures 9 d–9e. These three transitions with extended emission have smaller rotational quantum numbers with lower excitation energy levels of $E_u = 23$–89 K than the other transitions of $E_u > 374$ K which show spatially more compact distributions only detected around the continuum peak. Thus, the 213.427 GHz (1_1–0_0 E), 216.946 GHz (5_1–4_2 E), and 229.759 GHz (8_{-1}–7_0 E) lines could trace lower temperature and/or less dense extended components, such as shocked outflow–cloud interaction regions and outflow cavity walls (Cyganowski et al. 2017). The $^{13}CH_3OH$ line shows weak emission extending toward the north-west direction as seen in the moment 0 map (figure 9f), similar to the 229.759 GHz (8_{-1}–7_0 E) line.

The differences in moment 0 maps and channel maps of two selected methanol lines between Cycle 3 and Cycle 6 are shown in panels (c) and (f) of figures 6–8, respectively. There is an excess of the 229.589 GHz (15_4–16_3 E) line emission in the Cycle 6 data at the continuum peak C1 and slightly south-west of it, similar to the continuum map (figure 3c). This trend is common for all the methanol lines except for the 229.759 GHz (8_{-1}–7_0 E) line. The excess emission in Cycle 6 appears to be coincident with a localized patch of a slightly blueshifted emission seen in the moment 1 map (figure 6a).

3.4 Velocity structure of the methanol lines

Given the association of the 6.7 GHz class II methanol maser, G24.33+0.14 is thought to be an HMYSO associated with both outflow and possibly a circumstellar disk. As seen in moment 1 maps of the 229.589 GHz (15_4–16_3 E) line (figure 6a), a velocity gradient is evident along the north-east–south-west direction within the continuum source. On the other hand, the north-west–south-east outflow structure can be seen in the 229.759 GHz (8_{-1}–7_0 E) CH_3OH line within the velocity range of $\sim\pm10$ km s^{-1} with respect to the systemic velocity (figures 7 and 8).

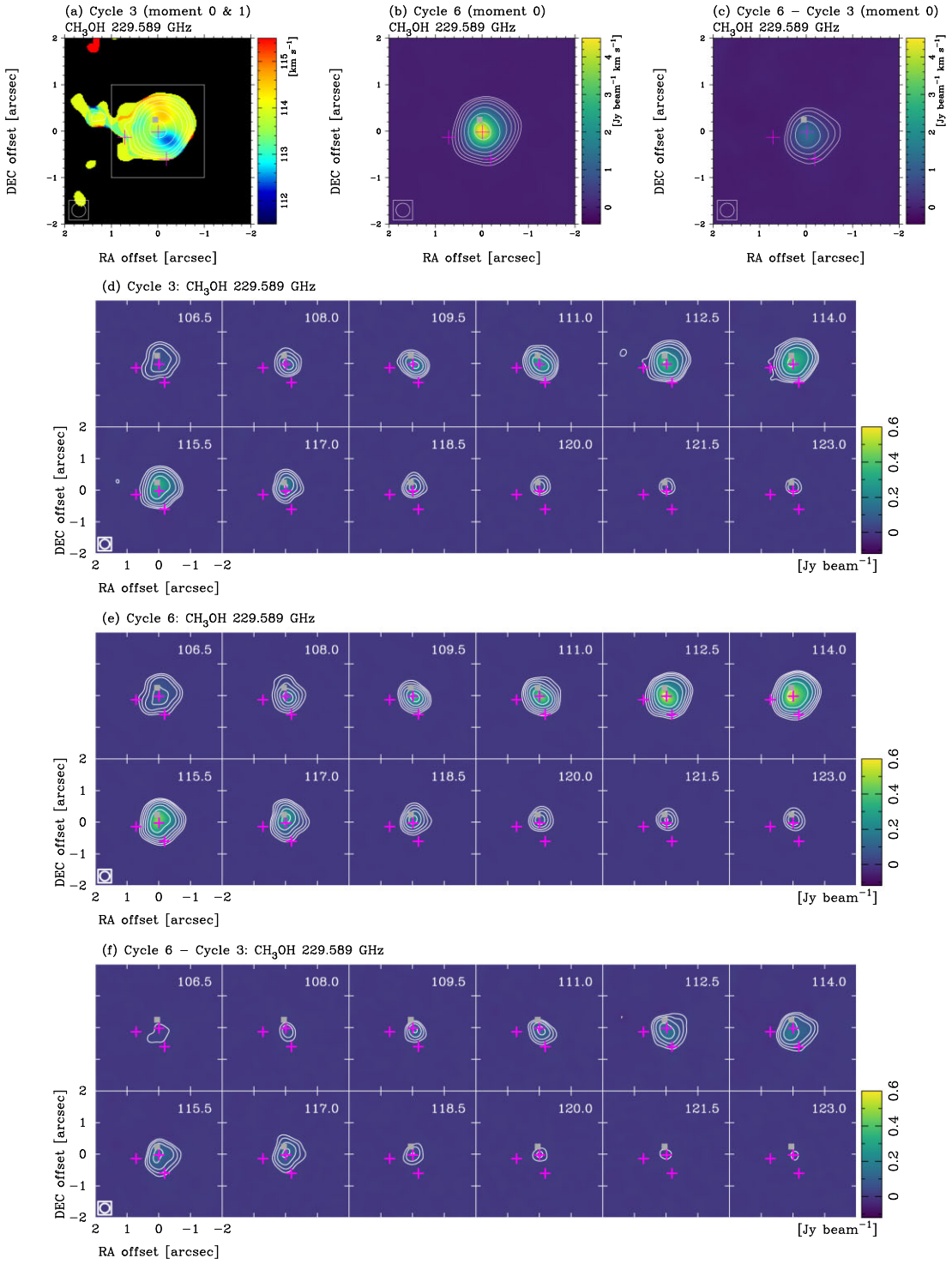

Fig. 6. (a) Moment 0 (white contour) and 1 (color scale) maps of the CH_3OH 229.589 GHz (15_4–16_3 E) line for the Cycle 3 data. The velocity range used for moment maps is from 108 to 120 km s^{-1}. Contour levels are -16, -8, -4, 4, 8, 16, ..., times the rms noise level of 18.7 mJy beam^{-1} km s^{-1}. These multiples (-16, -8, -4, 4, 8, 16, . . .) are the same in the following panels. Dashed contours indicate negative levels. The cutoff level in making the moment 1 map is 7.5 mJy beam^{-1} ($\sim 3\sigma$). The white box indicates the integrated region ($2'' \times 2''$) to extract molecular line spectra as plotted in figures 4 and 5. (b) Moment 0 (white contour and color scale) map of the CH_3OH 229.589 GHz (15_4–16_3 E) line for the Cycle 6 data. Contour levels are the multiples of the rms noise level of 13.4 mJy beam^{-1} km s^{-1}. (c) Differential image of the moment 0 maps between Cycle 3 and Cycle 6. Contour levels are the multiples of the rms noise level of 23.5 mJy beam^{-1} km s^{-1}. Color scales in panels (b) and (c) are the same. (d) Channel map of the CH_3OH 229.589 GHz (15_4–16_3 E) line for the Cycle 3 data with the velocity resolution of 1.5 km s^{-1}. Contour levels are the multiples of the rms noise level at the peak channel of 3.0 mJy beam^{-1}. (e) Same as panel (d) but for the Cycle 6 data. Contour levels are the multiples of the rms noise level at the peak channel of 2.0 mJy beam^{-1}. (f) Same as panel (d) but for the differential map between Cycle 3 and Cycle 6. Contour levels are the multiples of the rms noise level at the peak channel of 3.7 mJy beam^{-1}. Color scales in panels (d), (e), and (f) are the same. A magenta cross and gray square indicate the positions of the continuum peaks measured for the Cycle 6 data and the flaring 6.7 GHz methanol maser (A. Kobak in preparation), respectively.

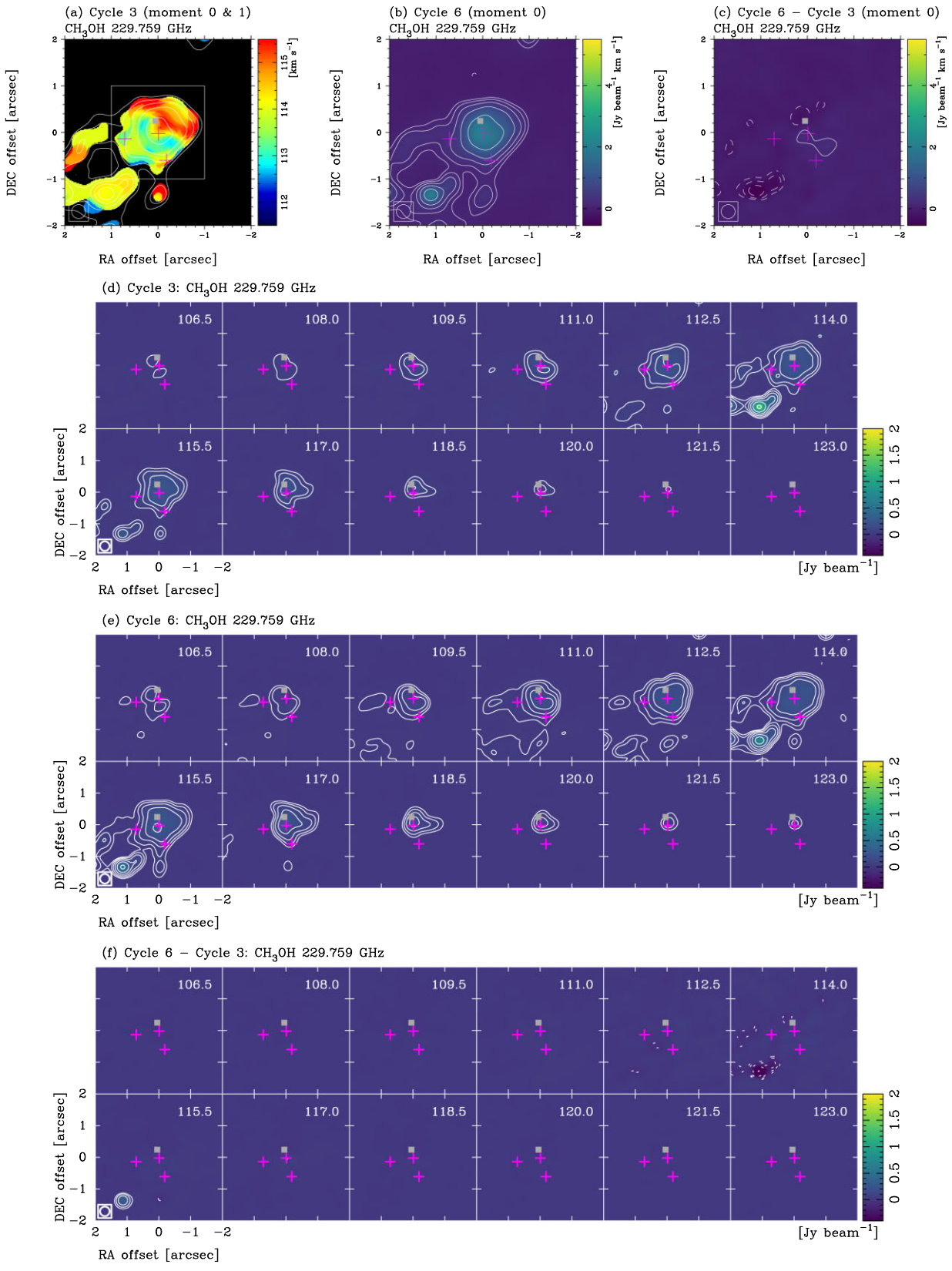

Fig. 7. Same as figure 6 but for the CH_3OH 229.759 GHz (8_{-1}–7_0 E) line. The multiples are the same as figure 6. (a) Contour levels are the multiples of the rms noise level of 25.9 mJy beam^{-1} km s^{-1}. The cutoff level in making the moment 1 map is 45 mJy beam^{-1}. (b) Contour levels are the multiples of the rms noise level of 21.3 mJy beam^{-1} km s^{-1}. (c) Contour levels are the multiples of the rms noise level of 31.8 mJy beam^{-1} km s^{-1}. (d) Contour levels are the multiples of the rms noise level at the peak channel of 10.1 mJy beam^{-1}. (e) Contour levels are the multiples of the rms noise level at the peak channel of 4.0 mJy beam^{-1}. (f) Contour levels are the multiples of the rms noise level at the peak channel of 11.0 mJy beam^{-1}.

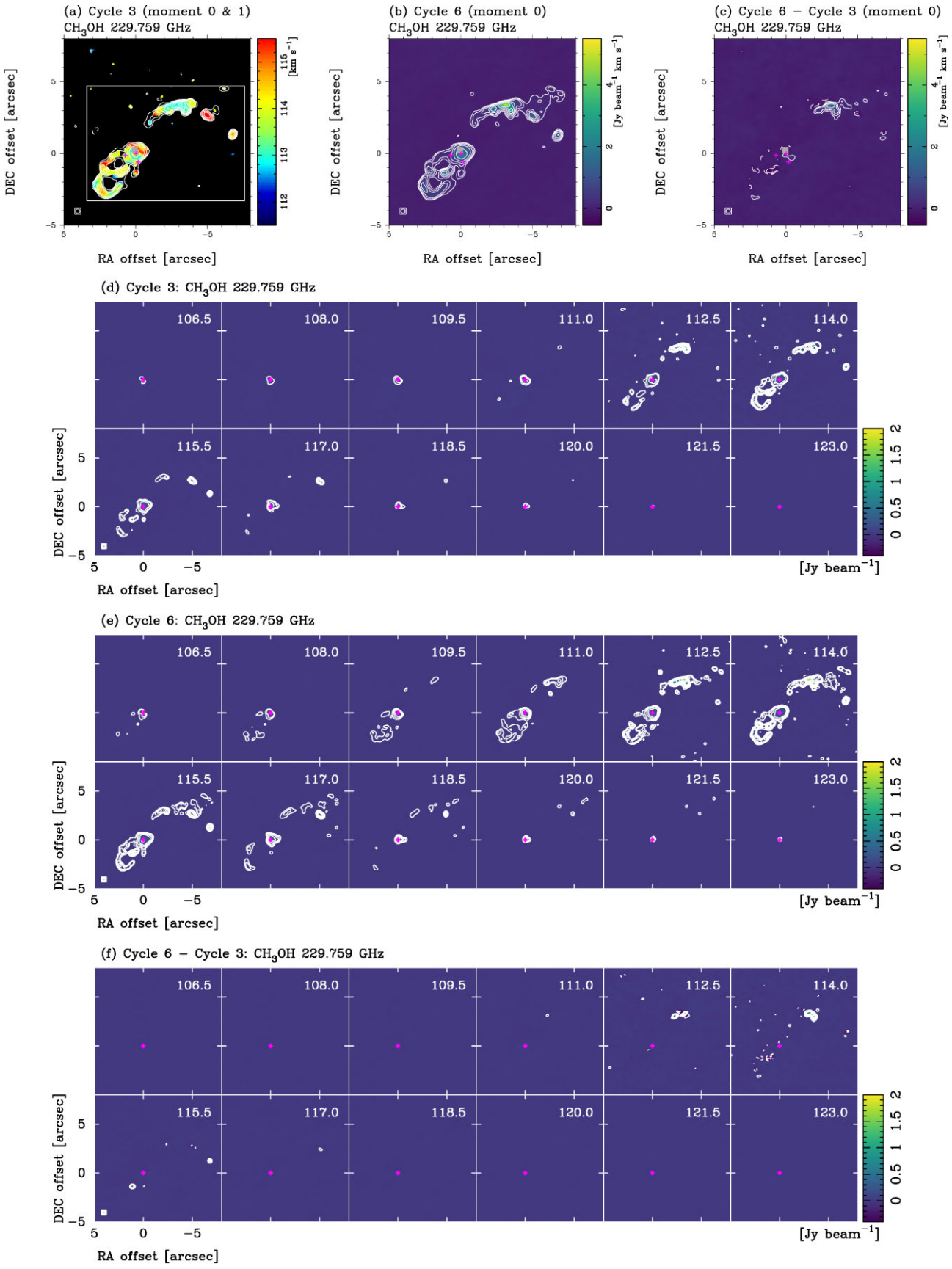

Fig. 8. Same as figure 7 but for a larger field of view. A white box in panel (a) indicates the integrated region (11″ × 8″) to extract molecular line spectra as plotted in figure 5.

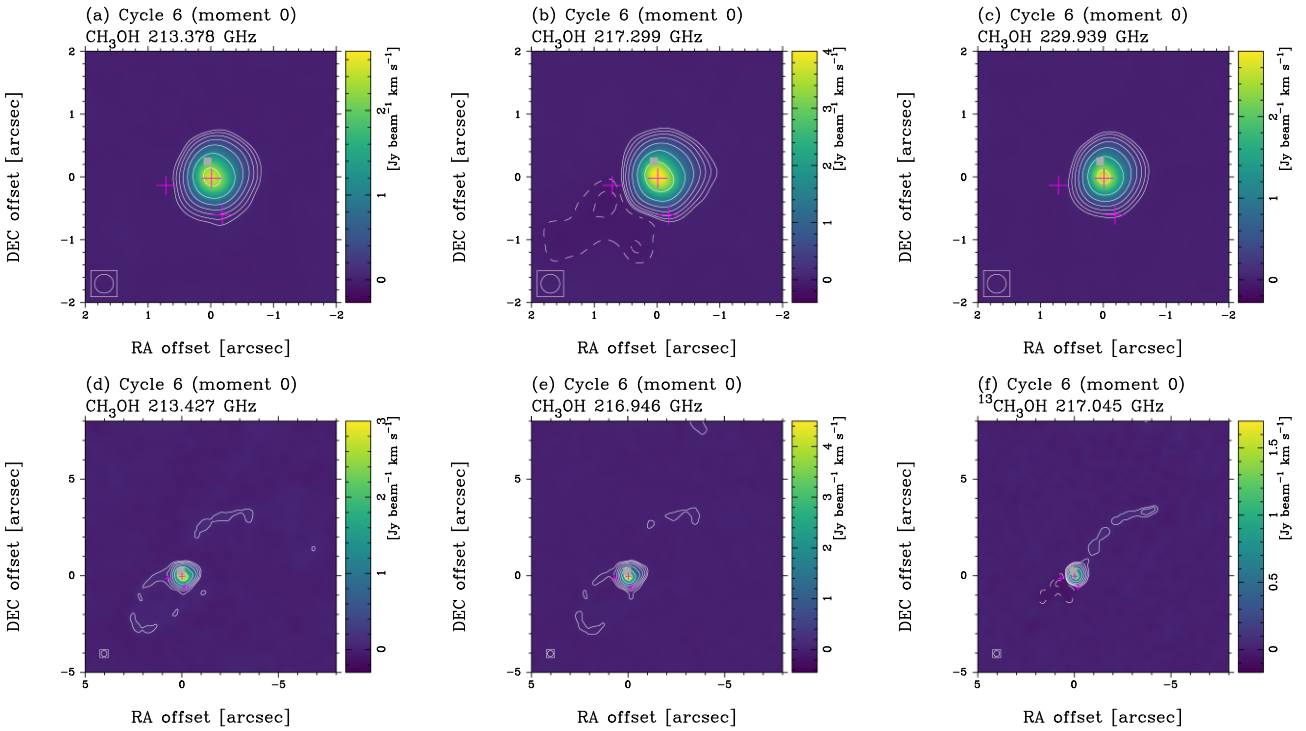

Fig. 9. Moment 0 maps (white contour and color scale) of the methanol lines for the Cycle 6 data. Contour levels are −16, −8, −4, 4, 8, 16, ..., times the rms noise levels indicated in parenthesis. (a) Central part of the 213.378 GHz (13_6–14_5 E) line image (8.6 mJy beam^{-1} km s^{-1}). (b) Same as (a) but for the 217.299 GHz ($v_t = 1$, 6_1–7_2 A$^-$) line (10.9 mJy beam^{-1} km s^{-1}). (c) Same as (b) but for the 229.939 GHz (19_5–20_4 A$^-$) line (9.4 mJy beam^{-1} km s^{-1}). (d) Wider field image of the 213.427 GHz (1_1–0_0 E) line (17.7 mJy beam^{-1} km s^{-1}). (e) Same as (d) but for the 216.946 GHz (5_1–4_2 E) line (13.5 mJy beam^{-1} km s^{-1}). (f) Same as (d) but for the ^{13}CH$_3$OH 217.045 GHz (14_1–13_2 A$^-$) line (8.2 mJy beam^{-1} km s^{-1}).

To investigate the dynamics of the central HMYSO in G24.33+0.14 located at the brightest continuum source C1, a velocity-centroid map was produced from the Gaussian fitting of the peak positions of channel maps as shown in the left-hand panel of figure 10. We used the whole UV range of the Cycle 6 data without smoothing the spectral channels in the imaging to achieve the higher spatial and spectral resolutions of ∼0.″2 and 0.5 km s^{-1}. The relative positional uncertainty of the fit in each channel map can be estimated from the ratio of beam-size/(2 × signal-to-noise ratio).

The velocity centroid map is compact, comparable to the synthesized beam size of the image (∼0.″2), and it shows possible signatures of the arc-like structure. Compared with other methanol lines, the 229.589 GHz (15_4–16_3 E) line shows the clearest evidence of the gradient along the northeast–southwest direction as seen in the moment 1 map. The position angle of the gradient is measured to be 15 ± 3° using the velocity centroid map presented in figure 10 (left).

Figure 10 (right) shows an example of the position–velocity (PV) diagram of the 229.589 GHz (15_4–16_3 E) line in Cycle 6 along the position angle of 15°. The linear velocity gradient is seen from 110 to 117 km s^{-1} centered at the peak LSR velocity of 113.5 km s^{-1}. Outside of this range, the velocity gradient becomes steeper with larger uncertainties. If the velocity gradient is caused by Keplerian rotation, the most blueshifted and redshifted velocity channels should be located close to the central position. However, figure 10 does not show such a trend, possibly because of insufficient spatial resolution which could obscure the central part of the disk, as demonstrated for another HMYSO Orion Source I (Ginsburg et al. 2018).

Alternatively, the linear velocity gradient can be expected if the emitting region shows a solid rotation or a rotating ring-like structure of the disk or envelope. In the case of a rotating ring with an edge-on geometry, the velocity gradient within the range of 110.0–117.0 km s^{-1} implies an enclosed mass of 8.8 ± 1.1 $M_\odot$ within the radius of 0.″09 (or 630 au). The above mass estimate would provide a lower limit, given the unknown inclination angle of the rotation axis. Furthermore, the velocity centroid maps could underestimate the derived mass due to insufficient angular resolution (Ginsburg et al. 2018). Further higher-resolution observations are crucial to unveil the more detailed dynamical structure of G24.33+0.14.

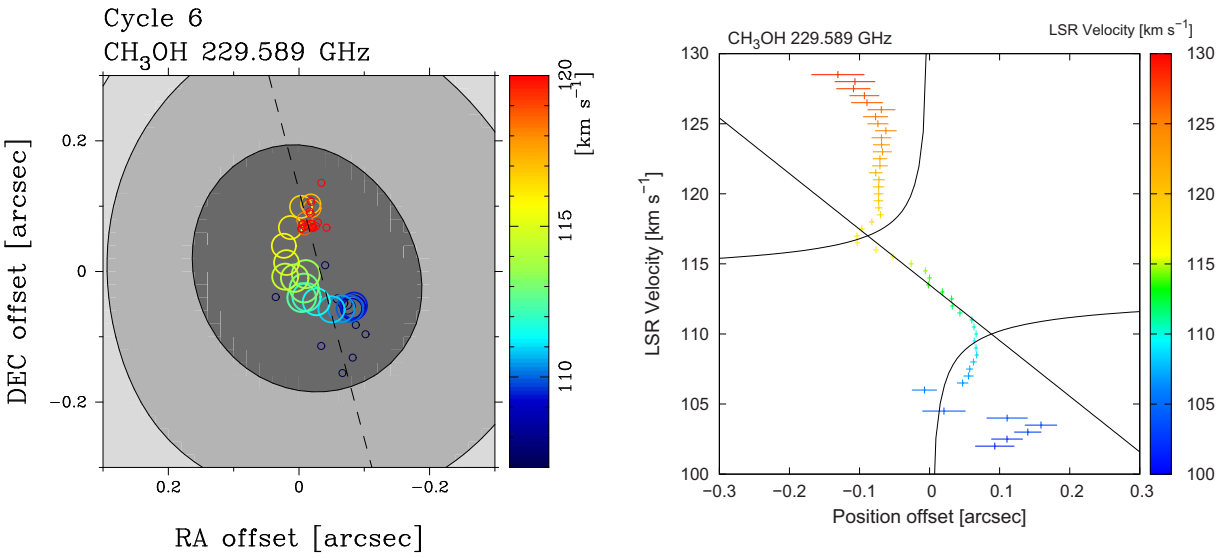

Fig. 10. (Left) Velocity-centroid map of the CH_3OH 229.589 GHz (15_4–16_3 E) lines in Cycle 6. The contours and gray-scale image show the moment 0 map. Peak intensities and positions are measured using the channel map produced with the whole UV range and the finer spectral resolution of 0.5 km s^{-1}. The size of each circle is proportional to the intensity. The dashed line indicates the position angle of the linear distribution of the centroid positions (15°). The (0, 0) position corresponds to RA = $18^h35^m08^s.140$ and Dec = $-07°35'04''.15$ (J2000.0). (Right) Position–velocity (PV) diagram of the CH_3OH 229.589 GHz (15_4–16_3 E) line for the Cycle 6 data produced from the velocity centroid map. The position offset is measured along the dashed line indicated in the velocity-centroid map (left-hand panel). A solid line shows the best-fitting linear velocity gradient between 110 and 117 km s^{-1}, with the enclosed mass of 8.8 $M_\odot$.

4 Discussion

4.1 Relationship between the 6.7 GHz methanol maser flare and accretion burst

As clearly seen in the light curves of the 6.7 GHz methanol masers (Wolak et al. 2019; A. Kobak in preparation) and the WISE/NEOWISE infrared emission at 4.6 μm (Wright et al. 2010; Mainzer et al. 2011), the flux variability in G24.33+0.14 shows clear correlation (figure 1). The maximum phase of the methanol maser flare is almost the same as the infrared peak. The 6.7 GHz methanol maser flux returned close to the pre-flare phase about half a year after the onset of the flare, as the IR emission decreased. Thus, the methanol maser flare in G24.33+0.14 strongly suggests a similar mechanism to those of other cases caused by episodic accretion events in S255IR NIRS3, NGC 6334I-MM1, and G358.93−0.03-MM1.

Our ALMA observations in Cycle 6 were conducted 20 days after the onset of the 6.7 GHz methanol maser flare and about one month (20–50 days) before its maximum phase, which lasted for about one month (figure 1). Although the WISE/NEOWISE infrared observations revealed the flux maximum at almost the same epoch as the 6.7 GHz methanol maser flare and our ALMA observation, there is a sign of only a marginal flux increase in the millimeter continuum emission by a factor of 1.16 with a calibration uncertainty of 10%. This is consistent with the previous studies for accretion burst sources, that the millimeter flux increase is smaller by an order of magnitude over the infrared bands (Johnstone et al. 2013; Contreras Peña et al. 2020; Stecklum et al. 2021). The 6.7 GHz methanol maser is pumped by strong infrared radiation close to the HMYSO (Cragg et al. 2005), and hence both are sensitive to the change in accretion luminosity. On the other hand, the millimeter continuum emission is mostly emitted from the more distant environment in the outer disk and/or dust envelope where changes in the dust and gas temperature propagate more slowly and with a smaller magnitude (Stecklum et al. 2021). Our follow-up observations of the millimeter continuum in G24.33+0.14 were carried out at the earliest phase among previous studies for S255IR NIRS3 and NGC 6334I-MM1, which is likely too early to heat the entire region of the disk/envelope around the HMYSO in G24.33+0.14. Therefore, the flux increase is smaller compared with the infrared emission from the central HMYSO.

In the case of S255IR NIRS3, the submillimeter continuum flux was higher by a factor of 2 about one year after the onset of the 6.7 GHz methanol maser flare than that in the quiescent phase (Liu et al. 2018), followed by a flux decrease after ∼2 yr from the flare (Hirota et al. 2021). Even two years after the onset of the flare, the flux densities of some of the 6.7 GHz methanol maser features were still higher by a factor of ∼10 at maximum than those in the quiescent phase (Szymczak et al. 2018b; Uchiyama et al. 2020; Hirota et al. 2021). The millimeter flare in

NGC 6334I-MM1 ∼1.5 yr after the start of the 6.7 GHz methanol maser outburst showed an increased flux density by a factor of 4 over the pre-flare phase (Hunter et al. 2017), and it has persisted for >6 yr (Hunter et al. 2021). During this active phase, the 6.7 GHz methanol maser also exhibits higher flux by one order of magnitude than that in the pre-flare phase (MacLeod et al. 2018; Hunter et al. 2021). On the other hand, another possible candidate for such an accretion burst source, G358.93−0.03-MM1, set an upper limit of ∼ 10% on the millimeter continuum flux increase observed in the three months after the onset of the methanol maser flare (Brogan et al. 2019; Stecklum et al. 2021). In G358.93−0.03-MM1, the active phase of the 6.7 GHz methanol maser flare lasted only $\lesssim$1 yr (Sugiyama et al. 2019).

As shown in figure 1, the methanol maser flare in G24.33+0.14 started from MJD∼58600 (2019 March). It returned to the quiescent level around MJD∼58900 (2020 January), and the duration of the maximum phase of the flare was MJD∼58770–58800 (2019 August–September). Because the methanol maser flare and infrared brightening in G24.33+0.14 did not last for long enough, it is suggested that the entire region of the disk and envelope could not be heated. Given the short active phase of the infrared flare in G24.33+0.14, the behavior would be similar to the case of G358.93−0.03-MM1 (Brogan et al. 2019; Stecklum et al. 2021). On the other hand, it is reported that the outburst of NGC 6334I-MM1 shows longer duration and larger energy by a factor of >3 compared with those of S255IR NIRS3 and G358.93−0.03-MM1 (Hunter et al. 2021). According to previous results, the accreted masses during the episodic events are 2 $M_{\rm Jup}$ and 0.6 $M_{\rm Jup}$ for S255IR NIRS3 (Caratti o Garatti et al. 2017) and G358.93−0.03-MM1 (Stecklum et al. 2021), respectively. The most recent SED fitting result for NGC 6334I-MM1 gives the mass accretion rate of $2.3 \times 10^{-3}\ M_\odot\ {\rm yr}^{-1}$, which would suggest the accreted mass of ∼0.01 $M_\odot$ or ∼10 $M_{\rm Jup}$ during 6 yr of the current outburst (Hunter et al. 2021). Thus, there are varieties in how the magnitude and duration of the luminosity change among the accretion burst sources. These differences are possibly attributable to a differing amount of accretion rate, accreted mass, and released energy (Stecklum et al. 2021).

It should be noted that the distances to the sources with significant flux increases (i.e., 1.78 kpc for S255IR NIRS3 (Burns et al. 2016) and 1.3 kpc for NGC 6334I-MM1 (Chibueze et al. 2014; Wu et al. 2014) are much closer than those without significant flux increase (6.75 kpc for G358.93−0.03-MM1 (Brogan et al. 2019) and 7.2 kpc for G24.33+0.14). This could imply that the millimeter continuum emission observed in the latter distant group tends to be emitted from the more distant environment compared to that in the former closer group. However, this is unlikely to be the major reason of the difference of two groups, because the linear resolution of G24.33+0.14 (0.″3 = 2200 au) smaller than that of S255IR NIRS3 (2″ = 3600 au) was used for the flux comparison.

4.2 Emission mechanisms of methanol lines

The peak brightness temperatures of all the methanol lines at the continuum peak C1 are 50–163 K, as listed in table 3. Based solely on the source size and brightness temperatures, it is unclear whether any of these transitions are masers. If maser emission is present, it is likely much more compact than our beam, so the observed brightness temperature would be diluted from the actual intrinsic value. Alternatively, the low brightness temperature would be explained if the emission is thermal or a mixture of thermal and maser components. In the latter case, the compact maser emission could be less than the thermal emission, and hence diluted.

As the spatial resolution of our ALMA data is still insufficient to resolve compact emission features, these beam-averaged brightness temperatures provide lower limits. For comparison, we produced synthesized images of the methanol lines for the Cycle 6 data using the whole *uv* range with uniform weighting. The beam size and the spectral resolution were ∼ 0.″2 and 0.5 km s^{-1}. If the emission is an unresolved maser, then the brightness temperature should increase by a factor of 2.25 over that of the 0.″3 resolution image. However, the peak brightness temperatures increased only by 6–38 K compared with those listed in table 3. The largest difference is seen for the 216.946 GHz (5_1–4_2 E) line, with a factor of 20% increase.

It should be noted that the methanol transition at 229.589 GHz (15_4–16_3 E) showed strong maser emission in another HMYSO G358.93−0.03-MM1, whose estimated distance of 6.75 kpc is slightly closer than that of G24.33+0.14 by a factor of 0.9 (Brogan et al. 2019). The brightness temperature of 4.82×10^3 K in G358.93−0.03-MM1 was much higher than that in G24.33+0.14, even though the spatial resolution was lower (∼ 0.″5) than those of the present study. Thus, we suggest that thermal emission is responsible for most or all of the flux from the observed methanol lines at the continuum peak of G24.33+0.14.

On the other hand, the brightest features of the 229.759 GHz (8_{-1}–7_0 E) line are distributed in the north-west and south-east lobes rather than at the continuum peak as can be seen in figure 8. The maximum intensities at the north-western peak of 1.55 ± 0.02 Jy beam^{-1} and 1.64 ± 0.01 Jy beam^{-1} in Cycle 3 and Cycle 6, respectively, are ∼6 times larger than that at the continuum peak position (table 3). If we use the Cycle 6 data with the spectral and spatial resolution of 0.5 km s^{-1} and 0.″2 for the full *uv* range data, the maximum intensity is measured to

be 3.26 ± 0.01 Jy beam^{-1} at the north-western peak, corresponding to a brightness temperature of 2600 K. This provides strong evidence of maser emission in this transition in G24.33+0.14. It is consistent with the previous results that this transition shows maser emission (Slysh et al. 2002; Cyganowski et al. 2011, 2012; Hunter et al. 2014; Kim et al. 2020). Other HMYSOs associated with EGOs, G11.92−0.61 and G19.01−0.03, show similar characteristics where the 229.759 GHz (8_{-1}–7_0 E) emission associated with the continuum sources is thermal, while the more extended emission is consistent with masers (Cyganowski et al. 2011). These characteristics are analogous to other class I methanol masers, such as the 44.1 GHz (7_0–6_1 A$^+$) maser line, where the emission peaks are offset from the continuum source and are located in outflow lobes traced by the extended 4.5 μm emission (Cyganowski et al. 2009).

4.3 Variability of the methanol and other molecular lines

As discussed in subsection 3.2, the millimeter methanol lines toward G24.33+0.14 show possible signatures of a systematic brightening trend in Cycle 6 compared with the other molecular lines and continuum emission. The mean flux density ratio (Cycle 6/Cycle 3) and its standard deviation of the methanol lines are 1.23 ± 0.13. In contrast, the other molecular lines show a smaller flux change with an average ratio and a standard deviation of 1.12 ± 0.15. This is comparable to that of the continuum emission of C1, 1.16 ± 0.01.

Here we point out that the changes in the flux densities of the methanol lines in G24.33+0.14 appear to depend on the excitation energy levels. As plotted in figure 11, the methanol lines with upper energy levels of $E_u > 370$ K showing the compact spatial distributions tend to have a ratio higher than those at lower excitation energies with more extended spatial structures. The averaged flux ratios for the methanol lines at higher and lower excitation energy levels are 1.33 ± 0.07 for four lines and 1.19 ± 0.01 for three lines [excluding the 229.759 GHz (8_{-1}–7_0 E) line], respectively. The latter is close to those of the other molecular lines, ranging from 19 K to 319 K. Another methanol line at 229.864 GHz (19_5–20_4 A$^+$) with a high excitation energy level of $E_u = 579$ K has the highest flux ratio of 1.45 ± 0.14 among the detected methanol lines, but it is excluded from table 3 due to the blending of the nearby $^{34}SO_2$ line.

We compare a possible correlation between the excitation energy levels and the flux ratios for 16 lines of four oxygen-bearing COMs such as $HCOOCH_3$, CH_3OCH_3, aGg'-$(CH_2OH)_2$, and $(CH_3)_2CO$, identified in our observations (table 4), and a similar trend is found as plotted in figure 11. While the trend is marginal, the correlation coefficient of 0.72 for the above four COMs is comparable to that for the eight methanol lines, excluding that at 229.864 GHz (19_5–20_4 A$^+$), of 0.65. The result should be taken with caution because of large error bars in each data point and an insufficient number of transitions to sample the range of excitation energy levels properly for each molecule.

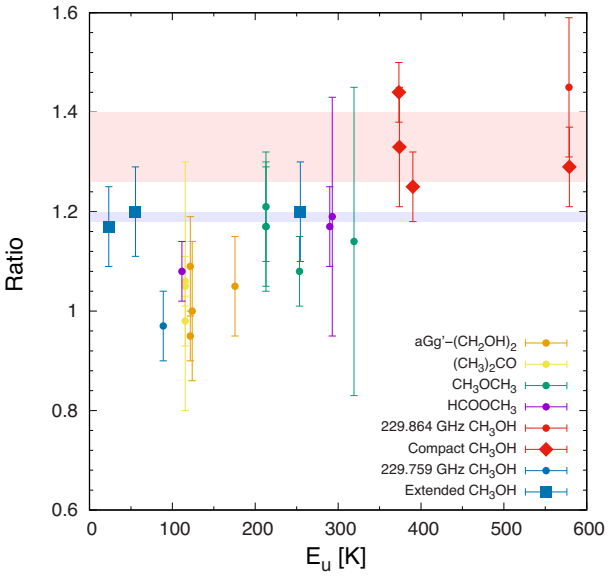

Fig. 11. Relationship between the flux ratios and excitation energies of the methanol and other COMs lines. The red and blue shaded areas show the average flux ratios including the errors (standard deviations) for the four compact methanol emission (red diamonds; 1.33 ± 0.07) and three extended methanol emission [blue squares; 1.19 ± 0.01, excluding the 229.759 GHz (8_{-1}–7_0 E) line], respectively.

If the flux ratios of low- and high-excitation methanol and COMs really show a systematic trend as a function of excitation energy levels, that would imply radiative heating around HMYSO due to an episodic accretion event. We will consider the following possibilities which cause the observed flux increases; (1) rise in the excitation temperature, (2) expansion of the emission region, (3) expansion of the methanol snowline, and (4) change in the emission mechanisms.

The rotational (excitation) temperature, T_{rot} can be expressed using the following equation (Turner 1991; Goldsmith & Langer 1999):

$$\log \frac{3kW}{8\pi^3 \nu S \mu^2 g_I g_k} = \log \frac{N}{Q_{rot}} - \frac{E_u \log e}{kT_{rot}}, \quad (1)$$

where W is the integrated intensity, ν is the frequency of the line, S is the intrinsic line strength, μ is the dipole moment, g_I is the nuclear spin weight, g_k is the degeneracy of the K-level, N is the column density, Q_{rot} is the partition function, and E_u is the upper state energy level. The best-fitting rotational temperatures of methanol of 213 ± 50 K and

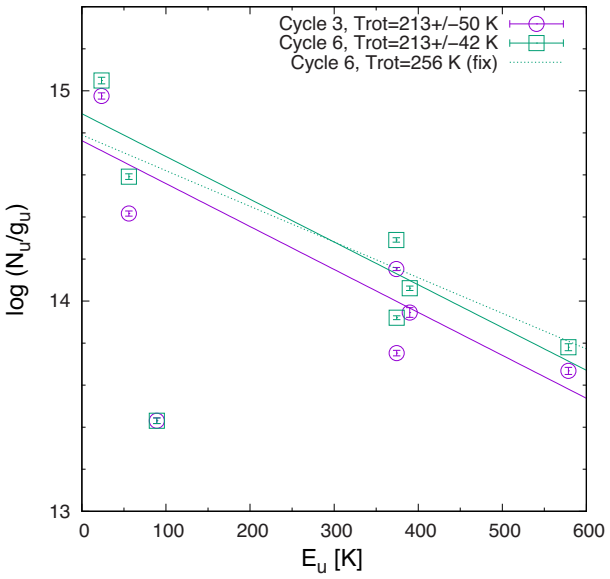

Fig. 12. Rotation diagram of the methanol lines in Cycle 3 (purple) and Cycle 6 (green) extracted from the 2″ × 2″ area around the continuum peak C1. Solid lines show the best-fitting results using the seven methanol lines for each epoch, excluding the 229.759 GHz (8_{-1}–7_0 E) line plotted at the bottom left-hand part of the panel. A dashed line is the fitting result for the Cycle 6 data with the fixed rotational temperature of 256 K (see subsection 4.3).

213 ± 43 K in Cycle 3 and Cycle 6, respectively, are in good agreement, as shown in figure 12, although the scatter in the diagrams is larger than the flux increase of each line, possibly due to high opacity and/or non-LTE (local thermal equilibrium) excitation conditions. For comparison, we plot the fitting results for the Cycle 6 data assuming the 20% higher rotational temperature of 256 K. While the result is still consistent within the large scatter, we could find no apparent change in the excitation temperature between the Cycle 3 and Cycle 6 data.

As discussed in the previous section (subsection 4.1), our Cycle 6 observations were taken well before the peak of the 6.7 GHz methanol maser light-curve (and thus of the infrared maximum), and the heating would be limited to the more compact region (Stecklum et al. 2021). If the beam filling factor of the methanol maser emission increases, the flux densities could show the increasing trend even without the temperature rise in the whole region within the beam. Assuming an expansion of the methanol emission region by 10% of the diameter of 0.″3 or 2160 au, which corresponds to a 21% increase of the filling factor, the expansion speed in 20 days would be 3% of the speed of light. A similar phenomenon was reported for the 6.7 GHz methanol maser flare in G358.93−0.03-MM1 (Burns et al. 2020), in which the maser distributions expanded from 260 au to 520 au in radius within 26 days after the accretion burst event, which corresponds to 4% of the speed of light.

It is also possible that evaporation of COMs from ice mantles on dust grains would expand the methanol snowline and enhance the beam-averaged methanol abundance when the dust temperature exceeds ∼100 K due to the increased radiation in an accretion burst event (Lee et al. 2019). The gas-phase abundances of various COMs including methanol are predicted to be enhanced after the accretion burst via both gas-phase chemistry and evaporation from ices by ∼2 orders of magnitudes or much larger, and to be kept overabundant for tens to hundreds of years compared with the pre-outburst phase (Molyarova et al. 2018). However, if G24.33+0.14 experiences accretion bursts in 2010–2012 (Wolak et al. 2018) at an interval of 8 yr (subsection 4.5), methanol and other COMs are unlikely to return to dust grains within such a short timescale. It should be noted that the theoretical model by Molyarova et al. (2018) is for low-mass FU Ori-type stars, and hence the luminosity and temperature would be much higher in the case of G24.33+0.14 even in the quiescent phase. The dust temperature in G24.33+0.14 would be too high to reform ice mantles on dust grains between an interval of the outburst events of 8 yr, and the gas-phase chemical abundances would be close to the steady state. Indeed, the beam averaged excitation temperature of 213 K is much higher than the evaporation temperature of methanol even before the flux increase. Thus, the flux increase would not be caused by the expansion of the snowline.

Alternatively, the larger flux increase seen in the higher-excitation methanol lines can be naturally explained if a part of the methanol emission comes from masers. It would explain the flux increase only for the methanol lines. In general, maser emission is more sensitive to the excitation conditions caused by the changes in the accretion luminosity and dust temperature (Cragg et al. 2005; Stecklum et al. 2021). Because masers often show rapid variation on short time-scales of an order of months (Moscadelli et al. 2017; Hunter et al. 2018; Burns et al. 2020), their preferred excitation and amplification conditions may have changed between Cycle 3 and Cycle 6. Differences in the flux density ratios from transition to transition could be due to different excitation conditions for masers (Slysh et al. 2002; Cragg et al. 2005). In fact, another example of a 6.7 GHz methanol maser flare in G358.93−0.03-MM1 showed drastic flux decreases in multiple millimeter masers from 199 to 361 GHz, differing by a factor of 3.0–7.2 within one month (Brogan et al. 2019). The lack of a strong flare in the 229.589 GHz (15_4–16_3 E) methanol maser unlike G358.93−0.03-MM1 (Brogan et al. 2019) may suggest a different degree of changes in physical conditions caused by the energetics of accretion bursts between G358.93−0.03-MM1 and G24.33+0.14. Considering the

possible flux increase of ∼20% in G24.33+0.14, contributions from any time-variable millimeter maser emission would be less significant in comparison with the strong 6.7 GHz class II methanol maser flare as discussed above (subsection 4.2). However, a smaller methanol maser flare of only a fraction of the emission could affect the observed flux change. For example, if 50% of the methanol emission is from a maser, then a 40% change in the maser component could explain a 20% change in total emission.

In summary, it is most likely that the possible systematic increasing trend of the methanol lines in G24.33+0.14 would be caused by radiative heating in the central part of the disk which results in expanding the size of the emission region within the beam and/or changes in the excitation condition. This is consistent with the fact that the gas heating in the entire disk and envelope is much smaller and slower than that of dust (Johnstone et al. 2013; Liu et al. 2020). If this is the case, the higher excitation lines which are selectively emitted from the inner/hotter region would have slightly higher impact on their line intensities. It is suggested that the extent of methanol transitions at higher excitation energy levels observed in the disk around another EGO source, G19.01−0.03-MM1, tend to show more compact structures (Williams et al. 2022). It is also consistent with our observational results that the methanol line widths are unchanged before and after the flux increase, where the expansion of the high-temperature region propagate outward in the disk with the lower rotation velocity region. The larger flux increases in the methanol lines than those of other COMs lines could be attributed to different molecular distributions and/or excitation mechanisms, i.e., possible contributions of masers. More detailed mechanisms will be investigated in future observational studies at higher spatial resolution in the next outburst event.

4.4 The 229.759 GHz class I methanol maser in the north-western lobe

As clearly seen in figure 8, the brightest features of the 229.759 GHz (8_{-1}–7_0 E) line are distributed in the north-west and south-east lobes rather than at the continuum peak within the narrow velocity range of $\sim\pm10$ km s^{-1}. Although a small fraction of HMYSOs show the 36.2 GHz (4_{-1}–3_0 E) and 44.1 GHz (7_0–6_1 A$^+$) class I methanol masers with large velocity offsets of >10 km s^{-1} (Voronkov et al. 2014), the millimeter thermal and maser transitions of methanol, including the 229.759 GHz (8_{-1}–7_0 E) class I maser, trace the low-velocity shocks only close to the systemic velocity as seen in the 44.1 GHz masers (Cyganowski et al. 2009). It has also been shown that another class I methanol maser line at 278.3 GHz (9_{-1}–8_0 E) trace shocked outflow–cloud interaction regions rather than the high-velocity, more collimated (more jet-like) gas traced by the ^{12}CO lines (Cyganowski et al. 2017).

The 229.759 GHz (8_{-1}–7_0 E) methanol maser emission reveals a structure suggestive of multiple bow shocks, in particular toward the south-eastern lobe in the 114 km s^{-1} channel. Multiple bow shocks with a separation of ∼2″ or ∼14000 au provide possible evidence for episodic ejection and accretion processes. Assuming a typical transverse velocity of the low-velocity outflows associated with class I methanol masers of 10 km s^{-1} (Cyganowski et al. 2009), one can estimate a dynamical timescale of 7000 yr for the formation of each bow shock. The assumed transverse velocity of 10 km s^{-1} is a reasonable lower limit because some other outflow sources associated with the 44.1 GHz class I methanol masers are found to have much higher velocities (Voronkov et al. 2010; Cyganowski et al. 2011, 2012, 2017). Thus, the timescale estimated above would be an upper limit.

Some of the strong features in the north-western lobe at the velocity range from 112.5 to 117.0 km s^{-1} (figure 8f) show brightening in the Cycle 6 data, while the flux ratio (Cycle 6/Cycle 3) of 1.16 at the position of the continuum peak C1 is less significant compared with other methanol transitions at the position of the continuum peak C1. Considering the dynamical timescale of the outflow, the flux density of this line would not be affected by the shock propagation of the low-velocity outflow. Furthermore, it is unlikely that the 229.759 GHz (8_{-1}–7_0 E) methanol line is pumped by the infrared radiation or heatwave (Burns et al. 2020), as the class I methanol masers are collisionally pumped in shocked regions. Thus, the 229.759 GHz (8_{-1}–7_0 E) maser emission would be stable over long periods of several years as seen for other class I methanol masers (Kurtz et al. 2004; Yang et al. 2020).

4.5 Implications of the repeating nature of the flare

Compared with the other accretion burst sources, S255IR NIRS3, NGC 6334I-MM1, and G358.93−0.03-MM1, G24.33+0.14 differs in that it has clearly shown a past methanol maser flare (Szymczak et al. 2018a; Wolak et al. 2018, 2019). Although NGC 6334I showed multiple methanol maser flares at least in 1999 and 2015, HMYSOs associated with the maser flares (i.e., NGC 6334I-MM1 or NGC 6334I-MM2) could not be identified in 1999 due to a lack of high-resolution observational data (MacLeod et al. 2018). As for S255IR NIRS3, only weak and irregular flares were reported (Szymczak et al. 2018a), while a relationship with the stronger methanol maser flare caused by the accretion burst in 2015 was still unclear.

The 6.7 GHz methanol maser light curve of G24.33+0.14 shows similar magnitudes in each of the flares (figure 1). Although the monitoring observations of the 6.7 GHz methanol maser in G24.33+0.14 were carried out by the Torun 32 m single-dish radio telescope with a beam size of 5′.8, its position was identified by higher-resolution interferometer observations before the flare in 2010–2012 (Caswell 2009; Xu et al. 2009; Breen et al. 2015). Because of a lack of any other millimeter continuum sources in our ALMA primary beam (27″) and any other known methanol masers within the single-dish beam of 6′ (Breen et al. 2015), it is likely that these two methanol maser flares were associated with the same HMYSO in the brightest continuum source C1.

As discussed for NGC 6334I (MacLeod et al. 2018), repeating maser flares could originate from successive periastron passages in a close binary system, which triggers the accretion events (Artymowicz & Lubow 1996). The previous maser flare in G24.33+0.14 occurred between 2010 and 2012 in which the maximum phase was recorded in mid-2011 (see figure 1). The interval between the flares is about 3000 d or 8 yr. If we simply assume Keplerian rotation with the mass of 8 $M_{\odot}$ estimated from the rotation curve of the methanol emission, the 8 yr periodicity would give the binary separation of 8 au or 1.1 ms at 7.2 kpc. The calculated radius is a lower limit because the enclosed mass is also a lower limit considering the unknown inclination angle of the rotation axis and insufficient resolution, which sometimes results in a smaller mass estimate (Ginsburg et al. 2018). We note that the weaker continuum sources C2 and C3 are unlikely to trigger the periodic burst in C1 by disk fragmentation or by binary interaction, given their large separations of 4000–5000 au.

G24.33+0.14 appears to exhibit evidence of two modes of episodic behaviors, involving a short-period 8 yr timescale which can be traced by the methanol maser flares, in addition to a 7000 yr timescale episodic outflow. Simulations of episodic accretion in HMYSOs predict frequent small bursts interspaced by less frequent and more intense bursts with similar ranges of timescales to those seen in G24.33+0.14 (Meyer et al. 2021). Thus, the temporal behavior of G24.33+0.14 would provide observational evidence supporting a bimodal or multi-modal episodic accretion in a single HMYSO.

If the methanol maser flare really has a periodicity of ∼3000 d, the next outburst event is expected in mid-2027. Measuring the interval of the multiple outburst events will allow us to estimate the orbital decay of the binary system as discussed for NGC 6334I (MacLeod et al. 2018). Some alternative mechanisms for periodic methanol maser flares have been proposed, such as periodic change of the seed photon flux and/or the pumping radiation field due to a colliding wind binary (van der Walt et al. 2009), an eclipsing binary (Maswanganye et al. 2015), periodic accretion on to a young binary system (Araya et al. 2010), or a rotating spiral shock in a circumstellar disk (Parfenov & Sobolev 2014). Another possible explanation of repeating flares without regular periodicity is an impulsive stellar flare (Fujisawa et al. 2012). It is proposed that some periodic variation of the methanol masers can be explained by stellar pulsation of HMYSOs (Inayoshi et al. 2013). This would not be the case for G24.33+0.14 as the periodicity of 3000 days requires a luminosity of $\sim 10^6\,L_{\odot}$, which is much larger than that estimated from the previous observations of $10^{4.7}$–$10^{4.8}\,L_{\odot}$ (Rathborne et al. 2011; Sánchez-Monge et al. 2013). Monitoring of both methanol masers and multi-band continuum emission from radio to infrared will provide novel information on changes in physical conditions between quiescent and mass accretion burst phases which are repeating on human timescales. Future long-term observations of this source should be initiated from the next quiescent phase in order to catch the next outburst.

5 Summary

Observations of millimeter continuum emission and methanol lines associated with the HMYSO G24.33+0.14 were carried out at ALMA Band 6 before (Cycle 3, 2016) and during (Cycle 6, 2019) the 6.7 GHz methanol maser flare in 2019. By using the same imaging parameters, such as the *uv* range, restoring beam size, and velocity resolution, the flux densities of eight methanol transitions and 26 other molecular lines from 13 molecular species were compared in the two epochs. The main conclusions are summarized below.

(1) In G24.33+0.14, three continuum cores, C1, C2, and C3, are identified. The continuum emission of the brightest peak, C1, in G24.33+0.14 shows only a marginal level of flux increase, by a factor of 1.16 ± 0.01, from Cycle 3 (2016 August) to Cycle 6 (2019 September), compared to the absolute flux calibration accuracy of 10%.

(2) Eight millimeter methanol emission lines, including one torsionally excited transition and one ^{13}C isotopologue, are detected, and one more methanol line is identified which is blended with the $^{34}SO_2$ line. They are divided into two types according to the spatial distributions; one is compact emission only around the C1 peak and the other is extended emission, showing components along the north-west–south-east outflow lobes.

(3) Millimeter methanol lines at the C1 position show velocity gradients along the north-east–south-west direction perpendicular to the outflow axis, implying the existence of a rotating disk or envelope with the enclosed mass of $>8\,M_{\odot}$.
(4) The millimeter methanol emission in G24.33+0.14 shows a possible signature of a systematic increase in flux density between Cycle 3 and Cycle 6 by a factor of 1.23 ± 0.13 on average with the absolute amplitude calibration uncertainties of 10%. The higher excitation methanol lines with compact structures tend to show larger flux increase. The systematic flux increase would suggest the radiative heating caused by an accretion event in the central part of the disk which could expand the size of the methanol emission and/or change the excitation conditions.
(5) The 229.759 GHz (8_{-1}–7_0 E) class I methanol masers trace multiple bow-shocks in the north-west–south-east outflow lobes indicative of episodic ejection with the timescale of $\lesssim$7000 yr. Along with the repeating nature of the 6.7 GHz methanol maser flare with an interval of 8 yr, G24.33+0.14 would suggest a bimodal or multi-modal episodic ejection, and hence accretion events. The high brightness temperature of 2600 K is strong evidence of maser emission as seen in some other HMYSOs.
(6) G24.33+0.14 is known as a hot molecular core, and 26 molecular lines from 13 molecular species other than methanol are identified. In addition to methanol, seven COMs are detected toward G24.33+0.14. There are only marginal flux changes in these non-methanol molecular lines with an average of 1.12 ± 0.15, which is comparable to that of the continuum emission.
(7) Considering the low brightness temperatures and small changes in the millimeter methanol lines, we find no clear evidence of a strong millimeter class II methanol line in G24.33+0.14. The lack of a strong millimeter methanol maser flaring, unlike G358.93−0.03-MM1, suggests different physical conditions among identified accretion burst sources.
(8) The flux change in the continuum emission in G24.33+0.14 is marginal and much smaller than those observed in some other methanol maser flares, such as for S255IR NIRS3 and NGC 6334I-MM1, but is comparable with another source G358.93−0.03-MM1. The characteristics in G24.33+0.14 could be explained by an episodic accretion burst event, possibly triggered by a close companion, but with smaller accretion luminosity and a shorter timescale than those in S255IR NIRS3 and NGC 6334I-MM1. Thus, the entire region of the envelope could not be heated in the accretion event in G24.33+0.14.

Due to the limited samples of variability studies in masers and continuum emission in high-mass star-forming regions, it is still premature to classify the type of variability seen in the continuum and maser emissions. Because the times of the observations for the various sources relative to the onset and/or peak of the burst are different, ranging from ∼1–3 months (G24.33+0.14 and G358.93−0.03-MM1) to ∼1–1.5 yr (S255IR NIRS3 and NGC 6334I-MM1), it is not easy to determine the start of the accretion burst events, which makes it difficult to compare strengths and timescales of the variabilities of masers and continuum emission accurately. Further long-term/dense monitoring at centimeter, millimeter, and infrared wavelengths will constrain the origin of the flux variation and possible relationship with mass accretion processes in HMYSOs including G24.33+0.14. Follow-up higher-resolution monitoring observations will reveal behaviors of time variation and emission mechanisms of the millimeter methanol lines along with other COMs lines. In addition, theoretical modeling of time-dependent chemical and physical properties during the accretion burst events are required for HMYSOs like S255IR NIRS3, NGC 6334I-MM1, G358.93−0.03-MM1, and G24.33+0.14 to interpret the observed properties. This source will provide unique opportunities to investigate mass accretion burst events possibly with an ∼8 yr periodicity; the next event is expected to occur in mid-2027.

Acknowledgments

We thank the anonymous referee for a helpful review, which has improved the manuscript. This paper makes use of the following ALMA data: ADS/JAO.ALMA#2015.1.01571.S and 2018.A.00068.T. ALMA is a partnership of ESO (representing its member states), NSF (USA), and NINS (Japan), together with NRC (Canada), NSC and ASIAA (Taiwan), and KASI (Republic of Korea), in cooperation with the Republic of Chile. The Joint ALMA Observatory is operated by ESO, AUI/NRAO and NAOJ. This publication makes use of data products from the Wide-field Infrared Survey Explorer (WISE), which is a joint project of the University of California, Los Angeles, and the Jet Propulsion Laboratory/California Institute of Technology, funded by the National Aeronautics and Space Administration. This publication also makes use of data products from NEOWISE, which is a project of the Jet Propulsion Laboratory/California Institute of Technology, funded by the Planetary Science Division of the National Aeronautics and Space Administration. TH is financially supported by the MEXT/JSPS KAKENHI Grant Numbers 17K05398, 18H05222, and 20H05845. MO is supported by Ministry of Education and Science of the Republic of Poland as part of support and granting funds for the Polish contribution to the International LOFAR Telescope (arrangement no. 2021/WK/02) and maintenance of the LOFAR PL-612 Baldy (MSHE decision no. 59/E-383/SPUB/SP/2019.1). RAB is supported by East Asia Core Observatory Association (EACOA) as an EACOA fellowship. ACG has been supported by PRIN-INAF-MAIN-STREAM 2017 "Protoplanetary disks seen through the eyes of new-generation instruments" and by PRIN-INAF 2019 "Spectroscopically tracing

the disk dispersal evolution (STRADE)". JSK has been supported by the Basic Science Research Program through the National Research Foundation of Korea (NRF) funded by the Ministry of Education (2016R1A5A1013277 and 2020R1A2C1007219). AMS was supported by the Large Scientific Project of the Russian Ministry of Science and Higher Education 'Theoretical and experimental studies of the formation and evolution of extrasolar planetary systems and characteristics of exoplanets' (No. 075-15-2020-780, contract 780-10). LU acknowledges support from the University of Guanajuato (Mexico) grant ID CIIC 164/2022. AV and LV are supported by Ministry of Science and Higher Education of the Russian Federation Grant 075-15-2020-780. Data analyses were in part carried out on common use data analysis computer system at the Astronomy Data Center, ADC, of the National Astronomical Observatory of Japan.

Appendix. Flux calibration

Absolute amplitude calibration is a critical issue to investigate flux variation of target sources. For the present dataset, the flux densities of the calibrators were compared with those being monitored by the ALMA Observatory.[9] All the flux-monitoring data are presented in figure 13 and table 5, along with our measured values. In the calibration, we assumed the flux densities at reference frequencies (F_0) and spectral index (spix) for flux calibrators taken from the regular monitoring by the ALMA Observatory through the CASA task SETJY. Based on these flux calibration data, we produced images of all calibrators. Their flux densities are measured by two-dimensional Gaussian fitting of the synthesized images ($F_{\rm obs}$).

One of the amplitude calibrators J1924−2914 was observed in the regular monitoring in 2019 September (Cycle 6) at Band 6 and the result was in good agreement with our observation (figure 13g). Although J1924−2914 was not observed in regular monitoring with ALMA Band 6 around our Cycle 3 observations in 2016 August, its flux densities determined by interpolating the Band 3 and Band 7 data is consistent with the long-term trend of the flux variation. On the other hand, another amplitude calibrator J1733−1304 (figure 13a) was not observed in the regular monitoring in 2016 August (Cycle 3) at Band 6. The flux density at Band 6 estimated by using Band 3 and Band 7 data was significantly higher (2.20–2.29 Jy) than those measured at Band 6 in 2016 September and May (1.65 Jy). The trend was coincident with the short-term flux increase at both Bands 3 and 7.

The boot-strapped flux density of a bandpass calibrator, J1751+0939, observed in Cycle 3 is in good agreement with that measured in the regular monitoring (figure 13b). Given the variation of the flux density values of three epochs of J1751+0939 observations ranging from 2.03 to 2.45 Jy, errors in the flux calibration in Cycle 3 would be

[9] ⟨https://almascience.nao.ac.jp/sc/⟩.

Table 5. Measured flux densities of calibrators.

Date	Flux calibrator	F_0* (Jy)	Spix†	$F_{\rm obs}$‡ (Jy)	Bandpass calibrator	$F_{\rm obs}$‡ (Jy)	Phase calibrator	$F^c_{\rm obs}$ (Jy)	Check source	$F_{\rm obs}$‡ (Jy)
2016 Aug 15	J1733−1304	2.342	−0.55943	2.286(2)	J1751+0939	2.452(2)	J1851+0035	0.2631(3)	J1827−0405	0.0305(5)
2016 Aug 19	J1924−2914	3.772	−0.64624	3.671(3)	J1751+0939	2.032(1)	J1851+0035	0.2412(2)	J1827−0405	0.0289(3)
2016 Aug 22	J1733−1304	2.245	−0.54528	2.196(2)	J1751+0939	2.360(2)	J1851+0035	0.2662(3)	J1827−0405	0.0326(4)
2019 Sep 25	J1924−2914	3.644	−0.51037	3.561(2)	J1924−2914	3.561(2)	J1832−1035	0.1747(2)	J1825−0737	0.0517(5)
2019 Sep 26	J1924−2914	3.643	−0.50120	3.568(2)	J1924−2914	3.568(2)	J1832−1035	0.1756(2)	J1825−0737	0.0489(6)

*Flux densities used for the flux scaling in the CASA task SETJY in the pipeline are assumed at the reference frequencies of 213.343 GHz and 213.337 GHz for Cycle 3 and Cycle 6 data, respectively.
†Assumed spectral index in the ALMA pipeline.
‡Flux density is measured by the two-dimensional Gaussian fitting using the AIPS task JMFIT. The numbers in parenthesis represent the fitting errors (1σ) in units of the last significant digits.

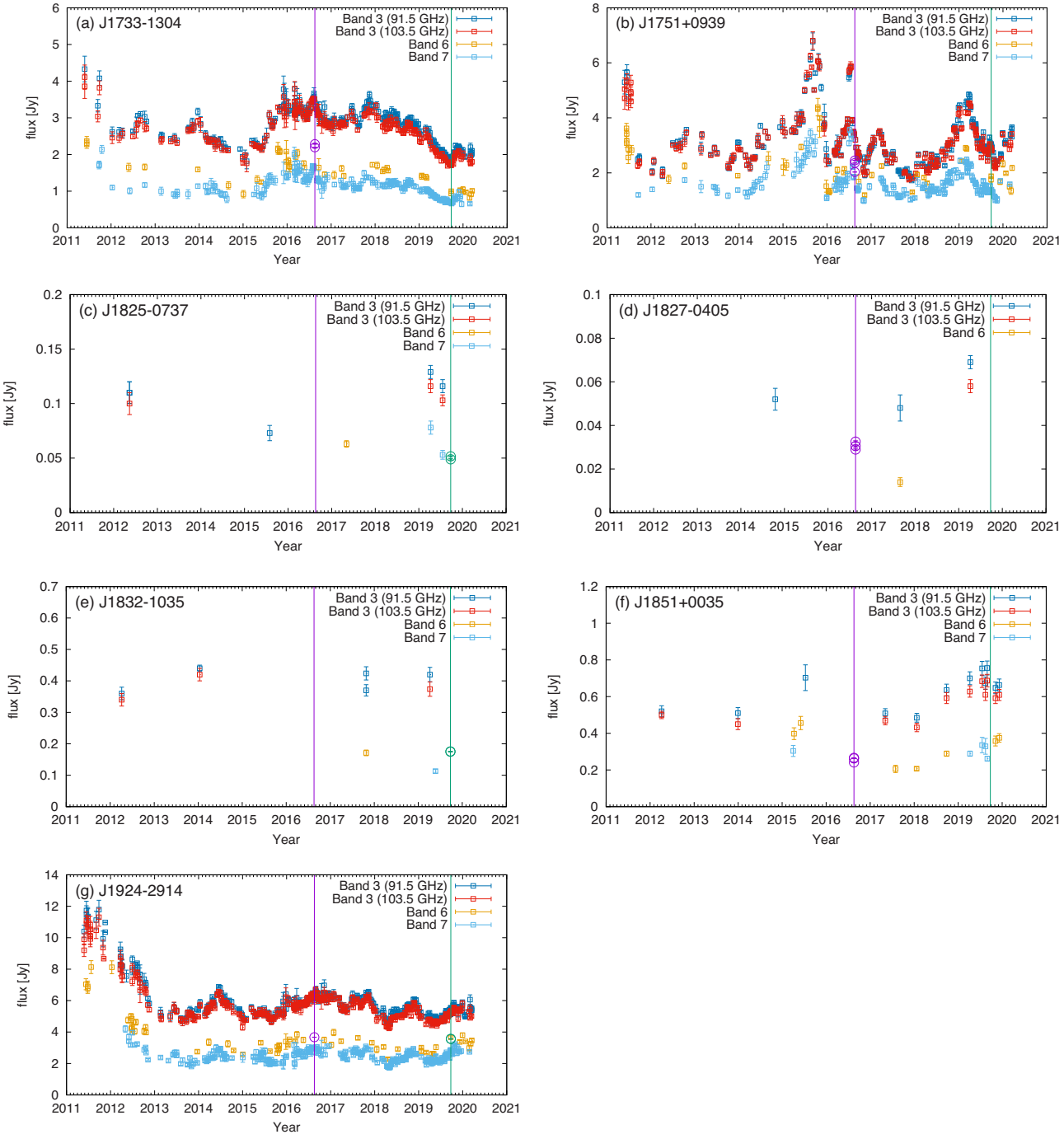

Fig. 13. Flux monitoring data for calibrators. Large open circles and small squares represent our measured values and those observed by the ALMA Observatory in regular monitoring, respectively. Purple and green vertical lines in 2016 August and 2019 September indicate the observed dates in Cycle 3 and Cycle 6, respectively.

~10%, which is the same level expected for the ALMA data.[10] It was not possible to compare boot-strapped flux densities of phase calibrators J1832−1035 (figure 13e) and J1851+0035 (figure 13f) directly, or check sources J1825−0737 (figure 13c) and J1827−0405 (figure 13d), because of the lack of monitoring data close to the observed dates (within a month), especially around 2019 September in Cycle 6. The catalogued values extrapolated in both frequency and dates provided by the ALMA pipeline differ by factors of 0.84–1.13 from those of measured values in Cycle 6. Thus, these tests are generally consistent with the

[10] ⟨https://almascience.eso.org/documents-and-tools/cycle6/alma-proposers-guide⟩.

expected absolute flux calibration uncertainty for ALMA of ∼10%.

References

Araya, E. D., Hofner, P., Goss, W. M., Kurtz, S., Richards, A. M. S., Linz, H., Olmi, L., & Sewiło, M. 2010, ApJ, 717, L133

Artymowicz, P., & Lubow, S. H. 1996, ApJ, 467, L77

Baek, G., Lee, J.-E., Hirota, T., Kim, K.-T., & Kim, M. K. 2022, ApJ, submitted (arXiv:2207.08223)

Bartkiewicz, A., Szymczak, M., & van Langevelde, H. J. 2016, A&A, 587, A104

Breen, S. L., et al. 2015, MNRAS, 450, 4109

Breen, S. L., Ellingsen, S. P., Contreras, Y., Green, J. A., Caswell, J. L., Stevens, J. B., Dawson, J. R., & Voronkov, M. A. 2013, MNRAS, 435, 524

Breen, S. L., Sobolev, A. M., Kaczmarek, J. F., Ellingsen, S. P., McCarthy, T. P., & Voronkov, M. A. 2019, ApJ, 876, L25

Brogan, C. L., et al. 2018, ApJ, 866, 87

Brogan, C. L., et al. 2019, ApJ, 881, L39

Burns, R. A., et al. 2020, Nature Astron., 4, 506

Burns, R. A., Handa, T., Nagayama, T., Sunada, K., & Omodaka, T. 2016, MNRAS, 460, 283

Caratti o Garatti, A., et al. 2017, Nature Phys., 13, 276

Caswell, J. L. 2009, PASA, 26, 454

Caswell, J. L., & Green, J. A. 2011, MNRAS, 411, 2059

Cesaroni, R., et al. 2018, A&A, 612, A103

Chambers, E. T., Jackson, J. M., Rathborne, J. M., & Simon, R. 2009, ApJS, 181, 360

Chen, X., et al. 2020, ApJ, 890, L22

Chen, X., Ellingsen, S. P., Shen, Z.-Q., Titmarsh, A., & Gan, C.-G. 2011, ApJS, 196, 9

Chen, Z., Sun, W., Chini, R., Haas, M., Jiang, Z., & Chen, X. 2021, ApJ, 922, 90

Chibueze, J. O., et al. 2014, ApJ, 784, 114

Chibueze, J. O., MacLeod, G. C., Vorster, J. M., Hirota, T., Brogan, C. L., Hunter, T. R., & van Rooyen, R. 2021, ApJ, 908, 175

Contreras Peña, C., Johnstone, D., Baek, G., Herczeg, G. J., Mairs, S., Scholz, A., Lee, J.-E., & JCMT Transient Team, 2020, MNRAS, 495, 3614

Cragg, D. M., Sobolev, A. M., & Godfrey, P. D. 2005, MNRAS, 360, 533

Cyganowski, C. J., et al. 2008, AJ, 136, 2391

Cyganowski, C. J., Brogan, C. L., Hunter, T. R., & Churchwell, E. 2009, ApJ, 702, 1615

Cyganowski, C. J., Brogan, C. L., Hunter, T. R., Churchwell, E., & Zhang, Q. 2011, ApJ, 729, 124

Cyganowski, C. J., Brogan, C. L., Hunter, T. R., Smith, R., Kruijssen, J. M. D., Bonnell, I. A., & Zhang, Q. 2017, MNRAS, 468, 3694

Cyganowski, C. J., Brogan, C. L., Hunter, T. R., Zhang, Q., Friesen, R. K., Indebetouw, R., & Chandler, C. J. 2012, ApJ, 760, L20

Cyganowski, C. J., Koda, J., Rosolowsky, E., Towers, S., Donovan Meyer, J., Egusa, F., Momose, R., & Robitaille, T. P. 2013, ApJ, 764, 61

Elbakyan, V. G., Nayakshin, S., Vorobyov, E. I., Caratti o Garatti, A., & Eislöffel, J. 2021, A&A, 651, L3

Fujisawa, K., et al. 2012, PASJ, 64, 17

Fujisawa, K., Yonekura, Y., Sugiyama, K., Horiuchi, H., Hayashi, T., Hachisuka, K., Matsumoto, N., & Niinuma, K. 2015, Astronomer's Telegram, 8286, 1

Ginsburg, A., Bally, J., Goddi, C., Plambeck, R., & Wright, M. 2018, ApJ, 860, 119

Goldsmith, P. F., & Langer, W. D. 1999, ApJ, 517, 209

Greisen, E. W. 2003, in Information Handling in Astronomy – Historical Vistas, ed. A. Heck (Dordrecht: Kluwer Academic Publishers), 109

Herbst, E., & van Dishoeck, E. F. 2009, ARA&A, 47, 427

Hirota, T., Cesaroni, R., Moscadelli, L., Sugiyama, K., Burns, R. A., Kim, J., Sunada, K., & Yonekura, Y. 2021, A&A, 647, A23

Hu, B., Menten, K. M., Wu, Y., Bartkiewicz, A., Rygl, K., Reid, M. J., Urquhart, J. S., & Zheng, X. 2016, ApJ, 833, 18

Hunter, T. R., et al. 2017, ApJ, 837, L29

Hunter, T. R., et al. 2018, ApJ, 854, 170

Hunter, T. R., et al. 2021, ApJ, 912, L17

Hunter, T. R., Brogan, C. L., Cyganowski, C. J., & Young, K. H. 2014, ApJ, 788, 187

Inayoshi, K., Sugiyama, K., Hosokawa, T., Motogi, K., & Tanaka, K. E. I. 2013, ApJ, 769, L20

Johns, K. P., Cragg, D. M., Godfrey, P. D., & Sobolev, A. M. 1998, MNRAS, 300, 999

Johnstone, D., Hendricks, B., Herczeg, G. J., & Bruderer, S. 2013, ApJ, 765, 133

Kim, J., et al. 2020, ApJ, 896, 127

Kurtz, S., Hofner, P., & Álvarez, C. V. 2004, ApJS, 155, 149

Lee, J.-E., et al. 2019, Nature Astron., 3, 314

Liu, S.-Y., Su, Y.-N., Zinchenko, I., Wang, K.-S., Meyer, D. M.-A., Wang, Y., & Hsieh, I.-T. 2020, ApJ, 904, 181

Liu, S.-Y., Su, Y.-N., Zinchenko, I., Wang, K.-S., & Wang, Y. 2018, ApJ, 863, L12

McCarthy, T. P., et al. 2022, MNRAS, 509, 1681

MacLeod, G. C., et al. 2018, MNRAS, 478, 1077

MacLeod, G. C., et al. 2019, MNRAS, 489, 3981

MacLeod, G. C., Smits, D. P., Green, J. A., & van den Heever, S. P. 2021, MNRAS, 502, 5658

McMullin, J. P., Waters, B., Schiebel, D., Young, W., & Golap, K. 2007, ASP Conf. Ser., 376, 127

Mainzer, A., et al. 2011, ApJ, 731, 53

Maswanganye, J. P., Gaylard, M. J., Goedhart, S., van der Walt, D. J, & Booth, R. S. 2015, MNRAS, 446, 2730

Menten, K. M. 1991, ASP Conf. Ser., 16, 119

Meyer, D. M.-A., Haemmerlé, L., & Vorobyov, E. I. 2019, MNRAS, 484, 2482

Meyer, D. M.-A., Vorobyov, E. I., Elbakyan, V. G., Eislöffel, J., Sobolev, A. M., & Stöhr, M. 2021, MNRAS, 500, 4448

Meyer, D. M.-A., Vorobyov, E. I., Kuiper, R., & Kley, W. 2017, MNRAS, 464, L90

Molyarova, T., Akimkin, V., Semenov, D., Ábrahám, P., Henning, T., Kóspál, Á., Vorobyov, E., & Wiebe, D. 2018, ApJ, 866, 46

Moscadelli, L., et al. 2017, A&A, 600, L8

Müller, H. S. P., Thorwirth, S., Roth, D. A., & Winnewisser, G. 2001, A&A, 370, L49

Ossenkopf, V., & Henning, T. 1994, A&A, 291, 943

Parfenov, S. Y., & Sobolev, A. M. 2014, MNRAS, 444, 620

Pickett, H. M., Poynter, R. L., Cohen, E. A., Delitsky, M. L., Pearson, J. C., & Müller, H. S. P. 1998, JQSRT, 60, 883
Proven-Adzri, E., MacLeod, G. C., van den Heever, S. P., Hoare, M. G., Kuditcher, A., & Goedhart, S. 2019, MNRAS, 487, 2407
Rathborne, J. M., Garay, G., Jackson, J. M., Longmore, S., Zhang, Q., & Simon, R. 2011, ApJ, 741, 120
Rathborne, J. M., Simon, R., & Jackson, J. M. 2007, ApJ, 662, 1082
Reid, M. J., Dame, T. M., Menten, K. M., & Brunthaler, A. 2016, ApJ, 823, 77
Sánchez-Monge, Á., López-Sepulcre, A., Cesaroni, R., Walmsley, C. M., Codella, C., Beltrán, M. T., Pestalozzi, M., & Molinari, S. 2013, A&A, 557, A94
Slysh, V. I., Kalenskiĭ, S. V., & Val'tts, I. E. 2002, Astron. Rep., 46, 49
Stecklum, B., et al. 2021, A&A, 646, A161
Stecklum, B., Caratti o Garatti, A., Hodapp, K., Linz, H., Moscadelli, L., & Sanna, A. 2018, in IAU Symp. 336, Astrophysical Masers: Unlocking the Mysteries of the Universe, ed. A. Tarchi et al. (Cambridge: Cambridge University Press), 37
Sugiyama, K., et al. 2019, Astronomer's Telegram, 12446, 1
Szymczak, M., Olech, M., Sarniak, R., Wolak, P., & Bartkiewicz, A. 2018a, MNRAS, 474, 219
Szymczak, M., Olech, M., Wolak, P., Gérard, E., & Bartkiewicz, A. 2018b, A&A, 617, A80
Turner, B. E. 1991, ApJS, 76, 617
Uchiyama, M., et al. 2020, PASJ, 72, 4
van der Walt, D. J., Goedhart, S., & Gaylard, M. J. 2009, MNRAS, 398, 961
Volvach, A. E., Volvach, L. N., Larionov, M. G., MacLeod, G. C., van den Heever, S. P., & Sugiyama, K. 2020, MNRAS, 494, L59
Voronkov, M. A., Caswell, J. L., Britton, T. R., Green, J. A., Sobolev, A. M., & Ellingsen, S. P. 2010, MNRAS, 408, 133
Voronkov, M. A., Caswell, J. L., Ellingsen, S. P., Breen, S. L., Britton, T. R., Green, J. A., Sobolev, A. M., & Walsh, A. J. 2012, IAU Symp. 287, Cosmic Masers - from OH to H0, ed. R. S. Booth et al. (Cambridge: Cambridge University Press), 433
Voronkov, M. A., Caswell, J. L., Ellingsen, S. P., Green, J. A., & Breen, S. L. 2014, MNRAS, 439, 2584
Williams, G. M., et al. 2022, MNRAS, 509, 748
Wolak, P., Olech, M., Szymczak, M., Bartkiewicz, A., & Durjasz, M. 2019, Astronomer's Telegram, 13080, 1
Wolak, P., Szymczak, M., Olech, M., & Bartkiewicz, A. 2018, IAU Symp, 336, Astrophysical Masers: Unlocking the Mysteries of the Universe, ed. A. Tarchi et al. (Cambridge: Cambridge University Press), 319
Wright, E. L., et al. 2010, AJ, 140, 1868
Wu, Y. W., et al. 2014, A&A, 566, A17
Xu, Y., Voronkov, M. A., Pandian, J. D., Li, J. J., Sobolev, A. M., Brunthaler, A., Ritter, B., & Menten, K. M. 2009, A&A, 507, 1117
Yang, W., Xu, Y., Choi, Y. K., Ellingsen, S. P., Sobolev, A. M., Chen, X., Li, J., & Lu, D. 2020, ApJS, 248, 18